RESEARCH ARTICLE | FEBRUARY 07 2019

Sound radiation by supersonic unstable modes in hypersonic blunt cone boundary layers. II. Direct numerical simulation

Carleton P. Knisely ; Xiaolin Zhong

Physics of Fluids 31, 024104 (2019)
https://doi.org/10.1063/1.5077007
CHORUS

Sound radiation by supersonic unstable modes in hypersonic blunt cone boundary layers. II. Direct numerical simulation

Cite as: Phys. Fluids 31, 024104 (2019); doi: 10.1063/1.5077007
Submitted: 23 October 2018 • Accepted: 10 December 2018 •
Published Online: 7 February 2019

Carleton P. Knisely[a] and Xiaolin Zhong[b]

AFFILIATIONS

MAE Department, University of California, Los Angeles, California 90095, USA

[a]Electronic mail: carleton.knisely@gmail.com
[b]Electronic mail: xiaolin@seas.ucla.edu

ABSTRACT

Supersonic modes, previously thought to be insignificant due to their smaller amplitude than Mack's traditional second mode, occur in hypersonic boundary layers when a disturbance travels supersonically with respect to the mean flow outside the boundary layer, causing outward-radiating acoustic waves. Very few previous studies perform Direct Numerical Simulation (DNS) of supersonic modes and instead rely on Linear Stability Theory (LST). This combined LST and DNS study investigates supersonic modes in Mach 5 flow over a blunt cold-wall cone. An LST analysis was performed in Paper I [C. P. Knisely and X. Zhong, "Sound radiation by supersonic unstable modes in hypersonic blunt cone boundary layers. I. Linear stability theory," Phys. Fluids **31**, 024103 (2019)], whereas DNS is the focus of Paper II. The overall goal is to determine the mechanism of supersonic modes and the conditions under which they exist. Compared to previous pure LST studies, DNS provides the advantage of making fewer limiting assumptions and can resolve interactions between modes. The results here indicate the excitation of supersonic modes via modal interactions not resolved with LST, suggesting the inadequacy of pure LST analyses concerning supersonic modes. Unsteady DNS results verified supersonic modes in the flow with wall-to-free-stream temperature ratio $T_w/T_\infty = 0.2$, lending credence to the modes' physical existence. However in the case of $T_w/T_\infty = 0.667$, sound radiation was also found in DNS while LST predicted a stable supersonic mode. The mechanism for supersonic modes is attributed to a modal interaction between mode F1, mode S, and the slow acoustic spectrum. Therefore, it is necessary to perform combined LST and DNS studies of supersonic modes to reliably predict their presence and impact on transition to turbulence.

I. INTRODUCTION

Hypersonic boundary layer transition is a critical area of study in the development of hypersonic vehicles. There is a drastic increase in drag and heating in the turbulent regime; therefore, accurately predicting the transition location can provide a better estimate in heat transfer to the vehicle. With this knowledge, the thickness and material of thermal protection systems (TPSs) can be more accurately specified, reducing the factor of safety in the TPS design, reducing the overall weight of the vehicle, and enabling a greater payload or vehicle range.

The major mechanism of transition to turbulence in hypersonic flows at zero angle of attack is receptivity to freestream disturbances leading to eigenmode growth. The dominant eigenmodes are known as Mack's first and second modes[1] although it should be noted that these instabilities are not distinctive modes in the mathematical definition.[2] To understand the behavior of these modes in direct numerical simulation (DNS), it is first necessary to understand their behavior under the linear disturbance amplitude assumption. In linear stability theory (LST), the perturbation in a flow variable q is described by a normal mode $q' = \hat{q}(y)\exp[i(\alpha x + \beta z - \omega t)]$, where $\hat{q}(y)$ is the eigenfunction, ω is the circular frequency of the disturbance, and α and β are the wavenumbers. For a 2D disturbance, $\beta = 0$. For comparison to a spatially developing disturbance wave in DNS, ω and β are assumed to be real, and the wavenumber α is assumed to be

complex which means the disturbances grow in space rather than time.

Mack's first mode is a viscous instability and can be completely stabilized by increasing the Mach number into the hypersonic regime. The second mode, however, is inviscid and is destabilized by increasing Mach number.[1] Therefore, in the hypersonic regime, Mack's second mode is the dominant instability wave. The second mode has been visualized as acoustic rays physically trapped between the wall and relative sonic line.[3–6] Mack[4] also notes that the second mode (and higher acoustic modes) is present whenever there is a region of local supersonic flow relative to the phase speed of the instability wave between the wall and the relative sonic point. Such a description of the second mode makes the assumption of a large wavenumber for a neutral mode and is not exact in reality.[4,7] However, this visualization has been invaluable to experimentalists and those performing DNS in understanding the structure of the second mode.

An illustration of the second mode inspired by previous authors[3–6] is shown in Fig. 1. This diagram also makes the same assumptions of large wavenumber for a neutral mode, although one would expect a qualitatively similar physical illustration for weakly non-neutral waves despite being quantitatively different. Including the imaginary component of the wavenumber can be thought of as a damping effect. The development of such a visualization of the second mode requires the understanding of the role of the sonic line described by the relative Mach number.

The complex local relative Mach number is given by

$$\overline{M}(y) = \frac{\overline{u}(y) - c}{\overline{a}(y)}, \tag{1}$$

where $\overline{u}(y)$ is the local mean flow velocity tangential to the wall, $c = \omega/\alpha$ is the complex disturbance propagation speed with ω being the circular frequency, α is the streamwise wavenumber, and $\overline{a}(y)$ is the local mean flow speed of sound. The real component of the phase speed is denoted as c_r. It can be shown[1] that $\overline{M}$ plays a significant role in the governing stability equations. Specifically, there is a turning point as $|\overline{M}|$ increases past unity. The solution of the second order ordinary differential equation (ODE) changes its behavior at the turning point, resulting in a different nature of the solution depending on the value of $\overline{M}$.

The relative sonic line, y_s, is then given by $\overline{M}(y_s) = -1$ in Fig. 1. The relative sonic line has also been denoted by previous authors[3–6] equivalently as $c = \overline{u}(y_s) + \overline{a}(y_s)$. More generally, the relative sonic line can be defined as any location where the magnitude of the real component of the relative Mach number is equal to unity, i.e., $|\text{Real}(\overline{M})| = 1$. Near the wall, the disturbance is propagating downstream supersonically ($\overline{M} < -1$) with respect to the local mean flow velocity. In this region where $\overline{M} < -1$, the stability equations are hyperbolic, resulting in the acoustic disturbance waves trapped by the wall with the relative sonic line acting as a wave guide in the large wavenumber limit. Outside of the $\overline{M} = -1$ turning point at $y = y_s$, the disturbance travels subsonically with respect to the free stream and creates a "rope-like" wave pattern observed by many researchers both experimentally[8,9] and numerically.[10–12] These structures are centered about $\overline{M}(y_c) = 0$, or equivalently $c = \overline{u}(y_c)$, with y_c denoting the critical layer. Because the phase speed of the mode is subsonic in the freestream, i.e., $\overline{M} < 1$, such a mode is referred to as a subsonic mode. The new illustration of the second mode in Fig. 1 is presented rather than the classical schematics[3–6] in preparation of a new illustration of the supersonic mode based on the same principles.

The nomenclature of Mack's first and second modes is not particularly descriptive, and as mentioned previously, the first and second modes are not actually distinctive modes.[2] In reality, there are multiple coexisting modes in the flow. The contemporary notation of Fedorov and Tumin[2] is used here instead with the following discussion relating Mack's description of the modes to the contemporary notation. Mack's first and second modes are known as discrete modes, which have a highly oscillatory eigenfunction within the boundary layer whose magnitude decays to zero sharply outside the boundary layer. Simultaneously existing in the flow are the continuous modes, whose eigenfunctions do not decay outside of the boundary layer. The four types of continuous modes are fast and slow

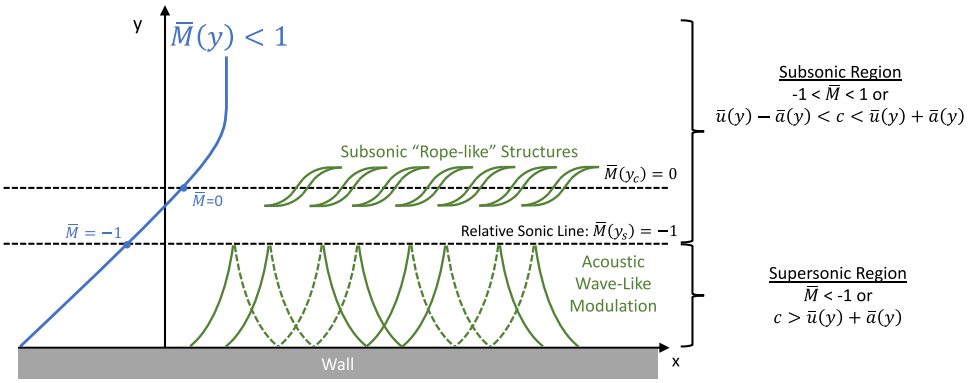

FIG. 1. Visualization of neutral second mode similar to Morkovin's,[3] Mack's,[4] Reshotko's,[5] and Fedorov's[6] assuming large wavenumber. The sonic line is denoted by $\overline{M}(y_s) = -1$ and the critical layer by $\overline{M}(y_c) = 0$. The reflection at the sonic line changes waves from compression to expansion and vice versa.

acoustic, entropy, and vorticity disturbances, although the entropy and vorticity spectra often overlap indistinguishably. Fedorov and Tumin's[2] notation for discrete modes includes a slow mode (mode S) and an infinite sequence of fast modes (mode F1, mode F2, etc.), also known to exist, as proposed by Mack.[1]

Mode S and mode F1 originate in the slow and fast acoustic spectra at the leading edge of the body. That is, mode S begins with a phase speed $c_r = 1 - 1/M_\infty$ and mode F1 begins with a phase speed of $c_r = 1 + 1/M_\infty$. In typical supersonic flows, the proximity of mode S to the slow acoustic spectrum can cause mode S to become unstable. This first unstable mode is referred to as Mack's first mode and is the compressible analog of Tollmien-Schlichting waves. In hypersonic flows, however, due to the increased Mach number, the viscous first mode instability is insignificant and can be completely stabilized. Further downstream from the leading edge, mode S increases in phase speed, while mode F1 decreases in phase speed. Eventually mode S and mode F1 synchronize, defined here as both modes having equal phase speeds, regardless of the growth rate. During synchronization, one mode can become unstable, while the other is stabilized.[2] Typically, mode S is the unstable mode, although in certain flow conditions mode F1 can become unstable instead.[13] Regardless of which mode is unstable, Mack's second mode refers to the unstable mode occurring after synchronization between mode F1 and mode S. Farther downstream, mode S can also synchronize with mode F2, mode F3, and higher modes to create Mack's third, fourth, and higher modes. However, the third and higher modes are decreasing in amplitude from the second mode;[1] therefore, the focus of the majority of hypersonic boundary layer transition studies is on the second mode.

The traditional second mode occurs when mode S is unstable after synchronization with mode F1, resulting in a subsonic phase speed, i.e., $1 - 1/M_\infty < c_r < 1 + 1/M_\infty$. In the cases when mode F1 becomes unstable after synchronization, its phase speed can become supersonic, i.e., $c_r < 1 - 1/M_\infty$ while unstable.[4,14] This situation results in a synchronization of mode F1 with the slow acoustic spectrum, causing a peculiarity in the eigenvalue spectrum due to the proximity of a discrete mode to a continuous mode. Downstream of this synchronization, the unstable mode F1 is referred to as the supersonic mode and is associated with unique features distinguishing it from the traditional second mode. Specifically, the supersonic mode is characterized by a second region of relative supersonic flow outside of the critical layer, resulting in the radiation of sound from the boundary layer.

The supersonic mode is not a new finding and has been studied since the 1980s. Numerical investigations by Mack in 1985[14] and 1990[4] and Reshotko in 1991[5] came to the consensus that the supersonic mode was insignificant due to its smaller disturbance amplification rate than the second mode. However, there has been a renewed interest in studying the supersonic mode in hypersonic boundary layers due to their presence in the flow conditions typical of the T5 shock tunnel at Caltech, largely sparked by the work of Bitter and Shepherd[15] in 2015. In such high-enthalpy shock tube experiments, the wall temperature remains ambient during the short test duration, resulting in a cold wall with respect to the free stream. Cold wall conditions in high-enthalpy flows are also found in some real flight cases.[16,17] It has long been known that wall cooling stabilizes the first mode but destabilizes the second mode.[14,18,19] Bitter and Shepherd's[15] work, however, took these cold-wall studies a few steps further and has shown through a chemical equilibrium, thermal nonequilibrium LST analysis that high levels of wall cooling on a flat plate lead to the supersonic mode. Their findings indicate that the supersonic modes are associated with instabilities over a wider range of frequencies than subsonic modes during which acoustic waves radiate from the wall into the free stream. This phenomenon has also been referred to as the spontaneous radiation of sound by Fedorov.[20,21]

Because of its perceived lack of impact on transition to turbulence, few studies have been performed, directly analyzing the supersonic mode. However, it has been encountered unexpectedly in many other studies.[22–28] Although DNS has rarely been used to study the supersonic mode, there is no lack of computational tools accounting for real gas effects that would be capable of resolving it. Candler[29] developed a thermochemical nonequilibrium DNS code for ionized hypersonic flow based on a shock-capturing approach. Similar well-known thermochemical nonequilibrium shock-capturing codes include US3D,[30] LAURA (Langley Aerothermodynamic Upwind Relaxation Algorithm),[31,32] and DPLR (Data-Parallel Line Relaxation).[33] In addition, Stemmer[34,35] used shock-capturing schemes with thermochemical nonequilibrium. Linn and Kloker[36] used a calorically perfect gas with thermal nonequilibrium in their DNS study. Ma and Zhong[37] used a two-temperature model with two species to simulate Mach 10 O_2 flow over a flat plate to reduce computational memory and cost. They incorporated chemical nonequilibrium, but assumed thermal equilibrium (i.e., the vibrational and translation-rotation temperatures were equal). In order to reduce the spurious oscillations behind the shock inherent to shock-capturing schemes, Prakash *et al.*[38] developed a high-order shock fitting method for thermochemical nonequilibrium flows and studied the receptivity of freestream disturbances. Parsons *et al.*[11] used the shock-fitting formulation with a 5-species thermochemical nonequilibrium air model to study the receptivity of freestream acoustic disturbances. Mortensen[39] expanded the study of thermochemical nonequilibrium effects to an 11-species air model incorporating surface chemistry. Overall, it was shown that chemical nonequilibrium has a significant destabilizing effect on second mode transition, while thermal nonequilibrium has a slight stabilizing effect.

A comprehensive examination of the supersonic mode's impact on transition to turbulence is yet to be performed

despite significant progress by a number of authors. In 1997 Chang, Vinh, and Malik[40] reported supersonic modes in Mach 20 chemical nonequilibrium, thermal equilibrium flow over a 6° wedge with wall temperature ratio T_w/T_{ad} = 0.1 and noted the stability boundary conditions in the free stream are critical to resolving the supersonic mode due to its oscillatory nature in the free stream. Additionally, they note that peak species perturbation coincides with the location of maximum chemical production in the boundary layer, and therefore the species eigenfunctions do not oscillate in the free stream, whereas pressure, temperature, and velocity perturbations exhibit the oscillatory behavior outside of the boundary layer. Bitter and Shepherd[15] in 2015 provided clear evidence through LST of the supersonic mode's existence on a cold-wall flat plate, although they neglected chemical nonequilibrium effects. Bitter and Shepherd also demonstrated that the cold wall was destabilizing to the supersonic mode. Over the course of 2014-2016, Salemi *et al.* also modeled the 5° half-angle sharp cone configurations typical of the T5 tunnel at Caltech and investigated second mode synchronization with the slow acoustic spectrum. They investigated the effect of nonlinear disturbances,[41,42] a flared cone geometry,[43] and high-temperature effects,[44] although the Prandtl number and the ratio of specific heats were fixed in their real gas model. Overall, Salemi[45] concluded that the synchronization of mode F1 with the slow acoustic spectrum caused the emission of acoustic waves from the boundary layer into the free stream. In 2016 Chuvakhov and Fedorov[20,21] largely confirmed Bitter and Shepherd's[15] findings through perfect gas LST analysis as well as unsteady DNS analysis on a flat plate, although they used different free stream conditions.

Edwards and Tumin[46] in 2017 found the supersonic mode on a hot wall with chemical effects, upending the notion that the supersonic mode occurs only on highly cooled walls. Edwards and Tumin incorporated additional source terms in their mean flow equations accounting for kinetic fluctuations in the flow, but used a perfect gas stability solver. Edwards and Tumin suggested that these kinetic fluctuations may generate a discrete mode in the vicinity of the neutral point. Depending on the flow parameters, the excited mode can become supersonic far downstream in the vicinity of the upper neutral branch curve. Therefore, the effect of wall temperature on the supersonic mode in thermochemical nonequilibrium flow must be re-evaluated. In 2018, Knisely and Zhong[47] performed thermochemical nonequilibrium LST and DNS studies using similar hot wall flow conditions on a 5° half-angle blunt cone and confirmed the existence of the supersonic mode, although it was quite weak. Knisely and Zhong[48] later in 2018 showed with unsteady DNS that the cold wall is destabilizing to the supersonic mode so much so that it is possible for the supersonic mode to have a greater magnitude than the traditional second mode. Furthermore, Mortensen[49] in 2018 discovered the supersonic mode in Mach 20 thermochemical nonequilibrium flow over very blunt cones and determined the supersonic mode to have a significantly higher amplitude than the second mode for nose radii greater than approximately 36 mm. Knisely and Zhong's[48] and Mortensen's[49] findings are novel and raise concerns of a dominant supersonic mode existing in other seldomly studied (but still practically relevant) flows. Therefore, a comprehensive examination of the supersonic mode's impact on transition to turbulence must be performed.

A schematic of a neutral supersonic mode (similar to the one developed by Knisely and Zhong[50]) is presented in Fig. 2 for further elaboration based on the same argument as the neutral subsonic second mode in Fig. 1, except a second relative sonic line is included. Specifically, it must again be noted that the visualization presented here is developed for the limiting case of a large wavenumber neutral mode, although there are qualitative similarities for finite wavenumber non-neutral modes. Nevertheless, it is indicative of the results one might expect to obtain from LST, DNS, or experiments in future studies. Near the wall, the same structures exist as in the traditional subsonic second mode. The disturbance is traveling supersonically downstream relative to

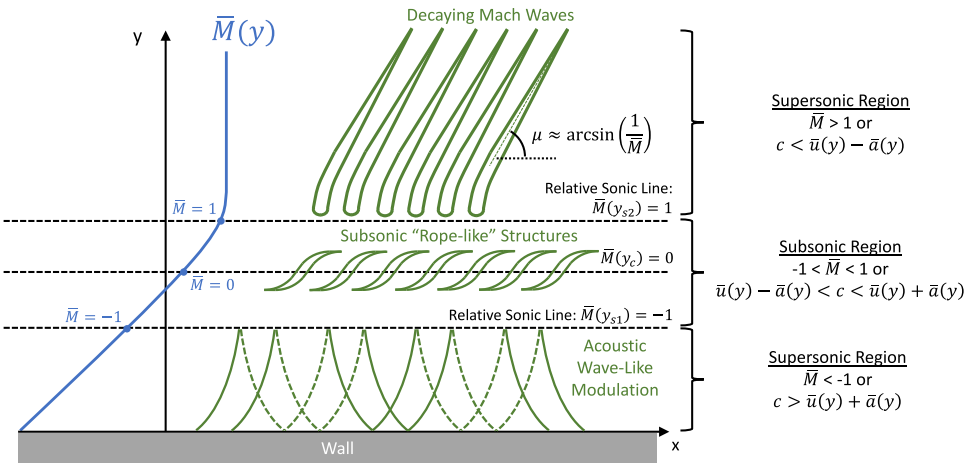

FIG. 2. Visualization of neutral supersonic mode in large wavenumber limit. The first sonic line is denoted by $\bar{M}(y_{s1}) = -1$, the critical layer by $\bar{M}(y_c) = 0$, and the second sonic line by $\bar{M}(y_{s2}) = 1$. The reflection at the first sonic line changes waves from compression to expansion and vice versa.

the mean flow, indicated below a relative Mach number of $\overline{M} < -1$, or equivalently $c > \overline{u}(y) + \overline{a}(y)$. The first sonic line $\overline{M}(y_{s1}) = -1$ again acts as a wave guide for the acoustic rays. Similar to the traditional subsonic second mode, outside of $\overline{M}(y_{s1}) = -1$, the disturbance is traveling subsonically with respect to the free stream and creates the "rope-like" wave pattern centered about the critical layer $\overline{M}(y_c) = 0$. When the phase speed of the disturbance is slow enough under very particular flow conditions, a second supersonic region can be present. There can exist a second relative sonic line $\overline{M}(y_{s2}) = 1$, or equivalently $c < \overline{u}(y_{s2}) - \overline{a}(y_{s2})$, outside of which the disturbance is traveling *upstream* supersonically with respect to the free stream. Again, because $|\overline{M}| > 1$, the solution to the stability equations are wave-like. This creates the "slanted" wave pattern outside of the boundary layer shown in the schematic in Fig. 2. As $y \to \infty$, the disturbance will reduce back to a pure acoustic wave. The angle created by this decaying wave pattern is analogous to a Mach wave angle from traditional compressible flow theory and is approximated by $\mu \approx \arcsin(1/\overline{M})$. For a neutral supersonic wave, this relation is exact. However because a non-neutral wave will have an imaginary component of the wavenumber, the Mach wave angle for a non-neutral instability will have a slightly different angle. Again, the schematic in Fig. 2 is simply an extension of the well-established visualization by previous authors for the traditional subsonic second mode in the large wavenumber limit[3–6] to include a second relative sonic line.

The results of Edwards and Tumin[46] and Knisely and Zhong[47] indicating that the spontaneous radiation of sound in hot-wall flows necessitates the re-evaluation of the role of wall temperature on the supersonic mode in nonequilibrium conditions. Furthermore, Knisely and Zhong[47,48] only observed the supersonic mode in DNS and not LST in their high-enthalpy flow, which raises questions regarding the mechanism of the creation of the supersonic mode. This two-part LST and DNS study performs a more in-depth analysis of the supersonic mode incorporating real gas effects on a blunt cone in conditions similar to Bitter and Shepherd.[15] The LST method and new shock boundary conditions have been verified in Paper I,[72] and the results indicate that the supersonic mode exists in the highly cooled conical flow with the wall-to-free-stream temperature ratio $T_w/T_\infty = 0.2$ and creates an abnormal growth pattern that is not observed in flows with traditional second-mode transition. However, the supersonic mode was not shown to exist using LST in the conical flow with $T_w/T_\infty = 0.667$.

Because Knisely and Zhong[47,48] suggest that the supersonic mode can be excited via a modal interaction, LST solvers will not resolve this excitation. Therefore, the use of DNS is necessary in combination with LST to fully determine the presence of the supersonic mode. The goals are to use thermochemical nonequilibrium DNS and LST analyses to (1) determine the characteristics of the supersonic mode and under what conditions it exists and (2) examine the impact of the supersonic mode on transition to turbulence under realistic flight or experimental conditions.

TABLE I. Freestream flow conditions for DNS simulations.

Parameter	Value	Parameter	Value
M_∞	5	$H_{0,\infty}$	9.17 MJ/kg
ρ_∞	2.322×10^{-2} kg/m^3	p_∞	10 kPa
T_∞	1500	U_∞	3882.42 m/s
c_{N_2}	0.78	c_{O_2}	0.22

II. SIMULATION CONDITIONS

The flow conditions for both simulations considered in this study are intended to be similar to those used by Bitter and Shepherd[15] and are summarized in Table I. The goal is to confirm that the DNS and LST methods are capable of producing the same physical artifacts on a blunt cone observed by Bitter and Shepherd[15] on a flat plate and expand on the results of Knisely and Zhong.[50] An in-depth LST study was performed in Paper I,[72] whereas the focus of Paper II is DNS. Two different mean flow cases are considered in this study; the only difference between the two cases is the isothermal wall temperature. All free stream conditions are identical. Case 1 had a wall temperature of $T_w = 300$ K, resulting in a wall-temperature ratio of $T_w/T_\infty = 0.2$. Case 2 had a wall temperature of $T_w = 1000$ K, resulting in a wall-temperature ratio of $T_w/T_\infty = 0.667$. The geometry is a 5° half-angle axisymmetric blunt cone which is 1 m in length with a nose radius of 1 mm. The DNS simulation used 256 points in the wall-normal direction and roughly 10 points/mm on the surface of the cone in the streamwise direction. In the azimuthal direction, four points are used. As will be explained in Secs. III and IV, the DNS code used in this study utilizes a shock-fitting method. Thus, the parameters in Table I are the free stream conditions upstream of the shock formed over the body.

III. GOVERNING EQUATIONS AND GAS MODEL

The governing equations for the DNS and LST codes are those developed by Mortensen and Zhong,[39,51–55] which are formulated for thermochemical nonequilibrium assuming a two-temperature model. Their formulation is presented here for clarity. The rotational mode is assumed to be fully excited with five non-ionizing species with finite-rate chemistry. Two-temperatures are used to represent translation-rotation energy and vibration energy. The five species model for air consists of N_2, O_2, NO, N, and O. Therefore, the Navier-Stokes equations in conservative form consist of five species mass conservation equations, three momentum conservation equations, and two energy equations: the total energy equation and the vibration energy equation. The governing equations in vector form are written as

$$\frac{\partial U}{\partial t} + \frac{\partial F_j}{\partial x_j} + \frac{\partial G_j}{\partial x_j} = W, \tag{2}$$

where U is the state vector of conserved quantities and W is the source terms defined by

$$\mathrm{U} = \begin{bmatrix} \rho_1 \\ \vdots \\ \rho_{ns} \\ \rho u_1 \\ \rho u_2 \\ \rho u_3 \\ \rho e \\ \rho e_v \end{bmatrix}, \quad \mathrm{W} = \begin{bmatrix} \omega_1 \\ \vdots \\ \omega_{ns} \\ 0 \\ 0 \\ 0 \\ 0 \\ \sum_{s=1}^{nms} (\mathrm{Q_{T\text{-}V,s}} + \omega_s e_{v,s}) \end{bmatrix}.$$

The inviscid and viscous flux vectors, F_j and G_j, respectively, are defined by

$$\mathrm{F}_j = \begin{bmatrix} \rho_1 u_j \\ \vdots \\ \rho_{ns} u_j \\ \rho u_1 u_j + p\delta_{1j} \\ \rho u_2 u_j + p\delta_{2j} \\ \rho u_3 u_j + p\delta_{3j} \\ (p + \rho e) u_j \\ \rho e_v u_j \end{bmatrix},$$

$$\mathrm{G}_j = \begin{bmatrix} \rho_1 v_{1j} \\ \vdots \\ \rho_{ns} v_{nsj} \\ \tau_{1j} \\ \tau_{2j} \\ \tau_{3j} \\ -u_i \tau_{ij} - k_T \frac{\partial T}{\partial x_j} - k_V \frac{\partial T_V}{\partial x_j} + \sum_{s=1}^{nms} \rho_s h_s v_{sj} \\ -k_V \frac{\partial T_V}{\partial x_j} + \sum_{s=1}^{nms} \rho_s e_{v,s} v_{sj} \end{bmatrix},$$

where v_{sj} is the species diffusion velocity and the viscous stress is defined as

$$\tau_{ij} = \mu \left(\frac{\partial u_i}{\partial x_j} + \frac{\partial u_j}{\partial x_i} \right) - \frac{2}{3} \mu \frac{\partial u_k}{\partial x_k} \delta_{ij}. \tag{3}$$

The total energy per unit volume, ρe, is defined as

$$\rho e = \sum_{s=1}^{ns} \rho_s c_{v,s} T + \rho e_v + \frac{1}{2} \rho \left(u_1^2 + u_2^2 + u_3^2 \right) + \sum_{s=1}^{ns} \rho_s h_s^o, \tag{4}$$

where the vibration energy per unit volume, ρe_v, is defined as

$$\rho e_v = \sum_{s=1}^{nms} \rho_s e_{v,s} = \sum_{s=1}^{nms} \rho_s \frac{\mathcal{R}}{\mathrm{M_s}} \frac{\theta_{v,s}}{\exp(\theta_{v,s}/T_V) - 1}, \tag{5}$$

where h_s^o is the species heat of formation, $\mathcal{R}$ is the universal gas constant, $\mathrm{M_s}$ is the species molecular weight, $e_{v,s}$ is the species specific vibration energy, and $c_{v,s}$ is the species translation-rotation specific heat at constant volume, defined as

$$c_{v,s} = \begin{cases} \frac{5}{2} \frac{\mathcal{R}}{\mathrm{M_s}} & s = 1, 2, \ldots, nms, \\ \frac{3}{2} \frac{\mathcal{R}}{\mathrm{M_s}} & s = nms + 1, \ldots, ns. \end{cases} \tag{6}$$

Additionally, $\theta_{v,s}$ is the characteristic vibrational temperature of each vibrational mode taken from Park.[56]

Chemical nonequilibrium is modeled by three dissociation reactions and three exchange reactions with each reaction governed by a forward and backward reaction rate determined from

$$k_f = \mathrm{C}_f \mathrm{T}_a^{\eta} \exp(-\theta_d / \mathrm{T}_a), \tag{7}$$

$$k_b = k_f / \mathrm{K}_{eq}. \tag{8}$$

The forward reaction rates, k_f, are obtained from Park.[56] The equilibrium coefficient, K_{eq}, is determined using a curve fit to experimental data from Park[56]

$$\mathrm{K}_{eq} = \mathrm{A}_0 \exp\left(\frac{\mathrm{A}_1}{\mathrm{Z}} + \mathrm{A}_2 + \mathrm{A}_3 \ln(\mathrm{Z}) + \mathrm{A}_4 \mathrm{Z} + \mathrm{A}_5 \mathrm{Z}^2 \right), \quad \mathrm{Z} = \frac{10\,000}{\mathrm{T}}. \tag{9}$$

The exchange between translation-rotation and vibration energies is governed by the Landau-Teller formulation

$$\mathrm{Q_{T\text{-}V,s}} = \rho_s \frac{e_{v,s}(\mathrm{T}) - e_{v,s}(\mathrm{T_V})}{\langle \tau_s \rangle + \tau_{cs}}, \tag{10}$$

where $\langle \tau_s \rangle$ is the Landau-Teller relaxation time from Lee.[57] The term τ_{cs} more accurately models the relaxation time in areas of high temperatures,[56] such as those occurring just downstream of the bow shock.

The Blottner[58] curve fit [Eq. (11)] is used to compute the viscosity of each species. Wilke's[59] mixing rule [Eq. (12)] is then used to compute the mixture viscosity, with the total heat conductivities for each energy mode computed in a similar fashion. A constant Schmidt number of 0.5 is used to compute the diffusion coefficient, which through Fick's law results in the diffusion velocity of each species

$$\mu_s = 0.1 \exp\left[(\mathrm{A}_s^{\mu} \ln(\mathrm{T}) + \mathrm{B}_s^{\mu}) \ln(\mathrm{T}) + \mathrm{C}_s^{\mu} \right], \tag{11}$$

$$\mu = \sum_{s=1}^{ns} \frac{\mathrm{X_s} \mu_s}{\phi_s}, \tag{12}$$

$$\mathrm{X_s} = \frac{\mathrm{c_s}}{\mathrm{M_s}}, \tag{13}$$

$$\phi_s = \frac{\sum_{r=1}^{ns} \mathrm{X_r} \left[1 + \left(\frac{\mathrm{M_s}}{\mathrm{M_r}} \right)^{1/4} \right]^2}{\left[8 \left(1 + \frac{\mathrm{M_s}}{\mathrm{M_r}} \right) \right]^{1/2}}. \tag{14}$$

IV. NUMERICAL METHODS

A. DNS

The thermochemical nonequilibrium code developed by Mortensen and Zhong[39,51–55] utilizes a high-order

shock-fitting method extended from a perfect gas flow version by Zhong[60] to compute the flow field between the shock and the body. The numerical method is repeated here for clarity. For shock-fitting computations, the shock location is not known *a priori*, so its position is solved along with the flow field. Since the shock position is not stationary, the grid used to compute the flow field is a function of time, leading to a coordinate transformation from physical (x, y, z, t) to computational (ξ, η, ζ, τ) coordinates. The governing equation can then be transformed into computational space as

$$\frac{1}{J}\frac{\partial U}{\partial \tau} + \frac{\partial E'}{\partial \xi} + \frac{\partial F'}{\partial \eta} + \frac{\partial G'}{\partial \zeta} + \frac{\partial E'_v}{\partial \xi} + \frac{\partial F'_v}{\partial \eta} + \frac{\partial G'_v}{\partial \zeta} + U\frac{\partial (1/J)}{\partial \tau} = \frac{W}{J}, \tag{15}$$

where J is the Jacobian of the coordinate transformation and

$$E' = \frac{F_1\xi_x + F_2\xi_y + F_3\xi_z}{J}, \tag{16}$$

$$F' = \frac{F_1\eta_x + F_2\eta_y + F_3\eta_z}{J}, \tag{17}$$

$$G' = \frac{F_1\zeta_x + F_2\zeta_y + F_3\zeta_z}{J}, \tag{18}$$

$$E'_v = \frac{G_1\xi_x + G_2\xi_y + G_3\xi_z}{J}, \tag{19}$$

$$F'_v = \frac{G_1\eta_x + G_2\eta_y + G_3\eta_z}{J}, \tag{20}$$

$$G'_v = \frac{G_1\zeta_x + G_2\zeta_y + G_3\zeta_z}{J}. \tag{21}$$

A seven point stencil is used to discretize the spatial derivatives

$$\frac{\partial f_i}{\partial x} = \frac{1}{hb_i}\sum_{k=-3}^{3}\alpha_{i+k}f_{i+k} - \frac{\alpha}{6!b_i}h^5\left(\frac{\partial f^6}{\partial^6 x}\right), \tag{22}$$

where

$$\alpha_{i\pm3} = \pm1 + \frac{1}{12}\alpha, \qquad \alpha_{i\pm2} = \mp9 - \frac{1}{2}\alpha,$$
$$\alpha_{i\pm1} = \pm45 + \frac{5}{4}\alpha, \qquad \alpha_i = -\frac{5}{3}\alpha,$$
$$b_i = 60,$$

and where h is the step size, $\alpha < 0$ is a fifth order upwind explicit scheme, and $\alpha = 0$ reduces to a sixth order central scheme. Here the inviscid terms use $\alpha = -6$ which yields a low dissipation fifth order upwinded difference ,and the viscous terms are discretized using $\alpha = 0$. The derivatives in the transverse direction, if required, are treated with Fourier collocation. To compute second derivatives, the first order derivative operator is applied twice.

Flux splitting is used for the inviscid flux terms resulting in

$$F' = F'^{+} + F'^{-}, \tag{23}$$

where

$$F'^{\pm} = \frac{1}{2}(F' \pm \Lambda U), \tag{24}$$

and Λ is a diagonal matrix that ensures F'^{+} and F'^{-} contain only pure positive and negative eigenvalues, respectively. For thermochemical nonequilibrium, the eigenvalues of Λ were derived by Liu and Vinokur.[61]

Conditions behind the shock are calculated from Rankine-Hugoniot relations. The free stream flow is assumed to be chemically frozen and in thermal equilibrium. The shock is assumed to be infinitely thin, meaning all relation occurs downstream of the shock as relaxation rates are finite. This leads to the chemical composition remaining constant across the shock, as well as the vibration temperature. A complete derivation of thermochemical nonequilibrium shock fitting can be found in Prakash *et al.*[38] A low storage 3rd-order Runge-Kutta method from Williamson[62] is used to advance the solution in time.

B. LST

The linear stability analysis used here has been described in detail in Paper I.[72] It is largely based on the LST code developed by Mortensen;[39] however, here the assumption of zero wall-normal velocity is relaxed (i.e., $\bar{v} \neq 0$), and new free stream boundary conditions incorporating a shock at the computational boundary are used. Curvature in the streamwise and transverse directions is included similar to Malik and Spall.[63] The LST equations are derived from the governing equations [Eq. (2)] where the instantaneous flow is comprised of a mean and fluctuating components, where the mean flow is assumed to satisfy the governing equations and is subtracted out. The mean flow is assumed to be a function of y only, and the flow disturbances are assumed to be small, i.e., linear. The perturbations are then assumed to be in the form of a normal mode described by $q' = \hat{q}(y)\exp[i(\alpha x + \beta z - \omega t)]$, where ω is the circular frequency of the disturbance and α and β are the wavenumbers. For comparison to DNS, the spatial stability approach is used, i.e., α is complex which results in the dispersion relation $\alpha = \Omega(\omega, \beta)$. Substituting in the normal mode form for the perturbation reduces the problem to a coupled set of $ns + 5$ ordinary differential equations

$$\left(\mathbf{A}\frac{d^2}{dy^2} + \mathbf{B}\frac{d}{dy} + \mathbf{C}\right)\vec{\phi} = \vec{0}, \tag{25}$$

where $\vec{\phi} = \left[\hat{\rho}_1, \hat{\rho}_2, \ldots, \hat{\rho}_{ns}, \hat{u}, \hat{v}, \hat{w}, \hat{T}, \hat{T}_V\right]^T$ and $\mathbf{A}$, $\mathbf{B}$, and $\mathbf{C}$ are complex square matrices of size $ns + 5$. This is now a boundary value problem where the derivative operators can be discretized using Lagrange polynomials in physical space, resulting in a 4th order method similar to the one used by Malik.[64]

Boundary conditions to solve the LST problem are required at the wall and in the free stream. At the wall, a high-order pressure extrapolation condition assuming zero mass flux from the wall and zero temperature perturbation are used, although more complex ablation boundary conditions can be used.[39] In the free stream, in flows in which the

supersonic modes are not a concern, all perturbations except $\hat{v}$ at the outer edge can simply be set to zero, and the $\hat{v}$ boundary condition is obtained from the continuity equation. However, in flows with supersonic modes, there is highly oscillatory eigenfunction behavior in the free stream. Using these zero-boundary conditions may not be physically relevant in this situation, especially when the boundary coincides with a shock. Therefore, free stream boundary conditions based on the Rankine-Hugoniot relations with a free shock approximation were derived, following similar methods as Chang *et al.*[40,65] Complete details of the derivation are presented in Paper I[72] and in Knisely and Zhong.[50]

V. STEADY FLOW FIELD SOLUTION

A. Case 1 steady flow field solution

Steady DNS translation-rotation temperature, vibration temperature, and mass fraction contours for the nose region of the cone are shown in Fig. 3. The upper half of Fig. 3(a) is the translation-rotation temperature, T, and the lower half is the vibration temperature, T_V. Figure 3(a) indicates that the flow is in thermal nonequilibrium in the nose region. Similarly, the mass fraction of N_2 and O_2 are shown in the upper and lower halves of Fig. 3(b), respectively. Figure 3(b) indicates that the flow is in chemical nonequilibrium. Specifically, O_2 dissociation is the predominant reaction in this flow field, whereas N_2 does not dissociate as severely.

Farther downstream, however, the chemical nonequilibrium effects weaken. Figure 4 shows the boundary layer profiles for temperature, vibration temperature, tangential velocity, and species density of N_2 and O_2 at a streamwise distance from the stagnation point of $s = 0.4$ m. Hereafter, y denotes the wall-normal distance. Due to the cold wall, the boundary layer is thin in relation to the flow domain. The mean flow does not reach thermal equilibrium in the free stream, thus demonstrating the necessity of accounting for nonequilibrium effects in these types of flows. The mass fractions of N_2 and O_2 follow the same trend in the boundary layer, but do not vary greatly in magnitude from their free stream values in these flow conditions. Although the effect of chemical

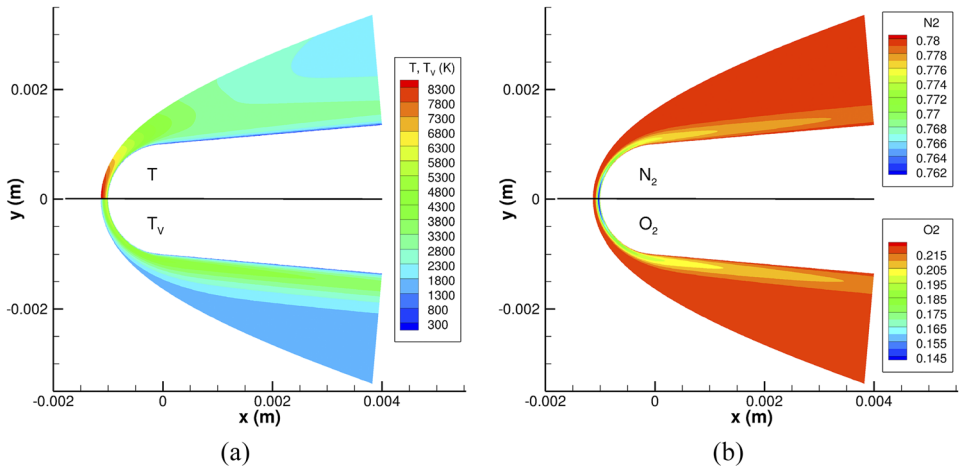

FIG. 3. Case 1 Steady flow field contours in nose region. (a) Upper half: T. Lower half: T_V. (b) Mass fraction of N_2 (upper half) and O_2 (lower half).

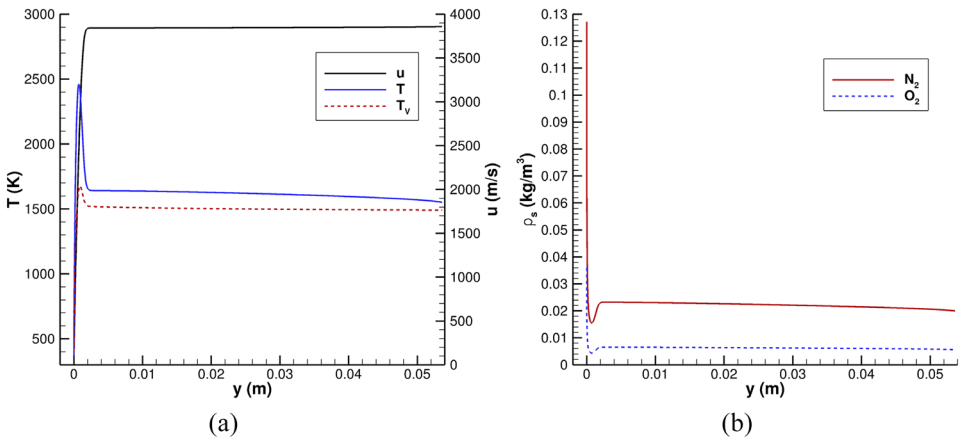

FIG. 4. Case 1 mean flow boundary layer profiles at $s = 0.4$ m. (a) u, T, and T_V. (b) Species density ρ_s of N_2 and O_2 species. u denotes the component of the velocity tangential to the surface of the cone. y is the wall normal distance.

nonequilibrium in the mean flow may be small, it may still have an effect in LST calculations.

B. Case 2 steady flow field solution

Similar to Case 1, the steady DNS translation-rotation temperature, vibration temperature, and mass fraction contours for the nose region of the cone are shown in Fig. 5. Because the only difference between Case 1 and Case 2 is the wall temperature, similar nonequilibrium effects occur in Case 2. Figure 5(a) indicates that the flow is in thermal nonequilibrium in the nose region, and Fig. 5(b) indicates that the flow is in chemical nonequilibrium. Again, O_2 dissociation

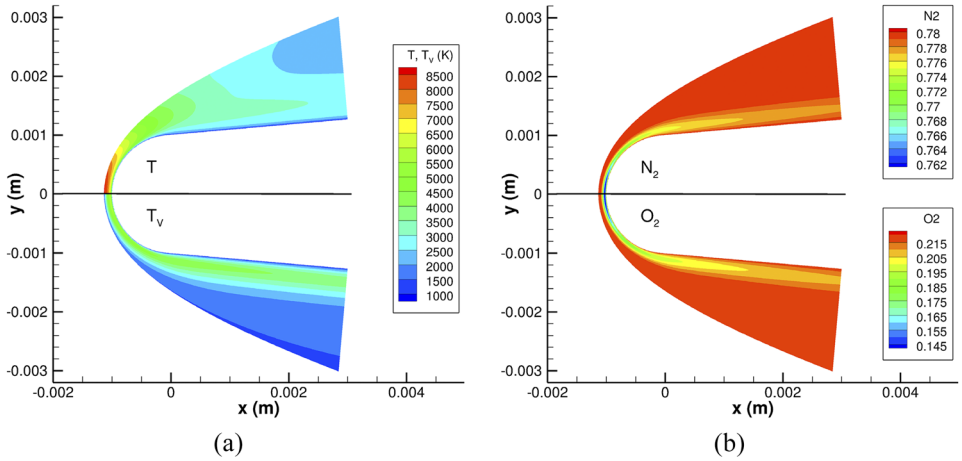

FIG. 5. Case 2 Steady flow field contours in nose region. (a) Upper half: T. Lower half: T_V. (b) Mass fraction of N_2 (upper half) and O_2 (lower half).

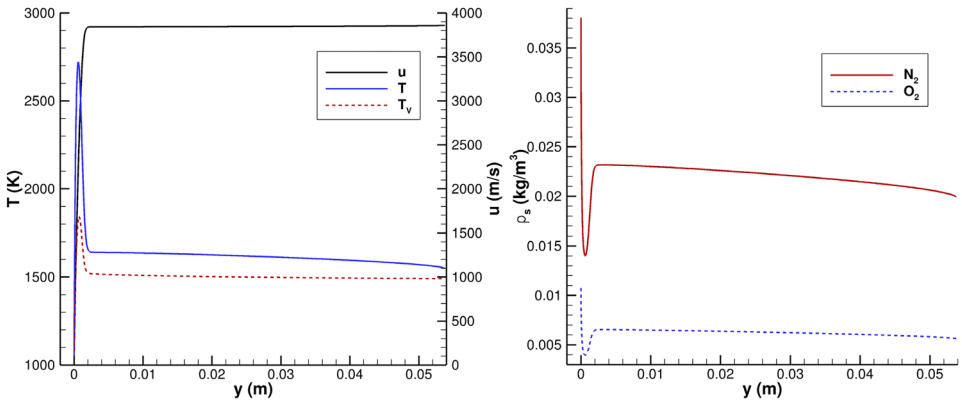

FIG. 6. Case 2 mean flow boundary layer profiles at s = 0.4 m. (a) u, T, and T_V. (b) Species density ρ_s of N_2 and O_2 species. u denotes the component of the velocity tangential to the surface of the cone. y is the wall normal distance.

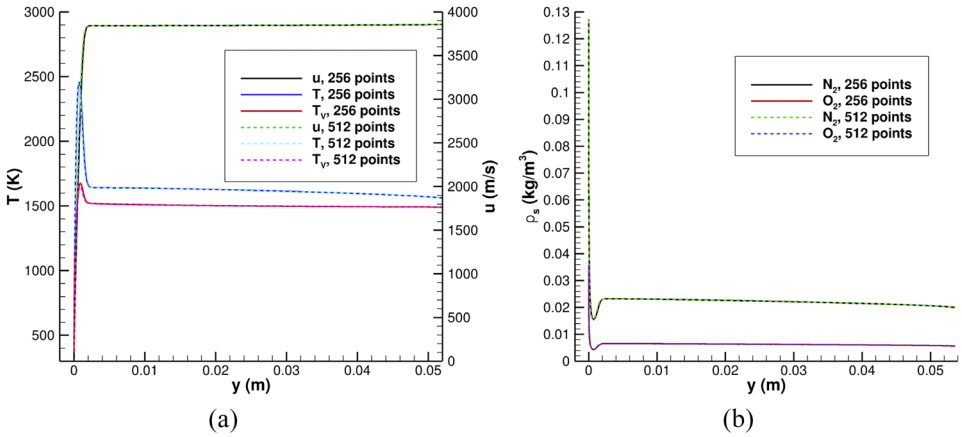

FIG. 7. Wall-normal grid point comparison of Case 1 mean flow boundary layer profiles at s = 0.4 m. (a) u, T, and T_V. (b) Species density ρ_s of N_2 and O_2 species.

TABLE II. Gaussian pulse parameters for DNS.

ϵ_b	μ_b	σ_b	x_b	l_b
1×10^{-4}	3×10^{-6}	4×10^{-7}	0.1 m	0.002 m

is the predominant reaction in this flow field, whereas N_2 does not dissociate as severely.

Farther downstream, the boundary layer profiles (Fig. 6) indicate that Case 2 is in thermal nonequilibrium in the free stream, similar to Case 1. However, the species density of N_2 appears to deviate more than in Case 1, suggesting that chemical effects play a larger role in the free stream in Case 2.

C. Steady flow field solution grid independence

The steady flow field grid points in the wall-normal direction for Case 1 were doubled to 512 points from 256 to determine the number of grid points required for a grid-independent solution. The wall-normal grid density is known to be much more critical than the wall-tangent grid density. Mean flow boundary layer profiles at s = 0.4 m (Fig. 7) indicate very little difference in the mean flow profiles when the grid is doubled. Furthermore, doubling the grid for the steady flow field solution significantly increased the computational expense to obtain a converged solution. Therefore, 256 grid points in the wall-normal direction was sufficient to provide an accurate solution.

VI. UNSTEADY DNS RESULTS

To study stability using DNS, it is required that the mean flow be perturbed in order to study the growth, or decay, of the perturbation. Here, the flow is perturbed with a suction/blowing slot at the cone surface. The equation for the mass flux of the slot is

$$\rho v(x,t)'_w = \epsilon_b(\rho u)_\infty \exp\left\{-\frac{(t-\mu_b)^2}{2\sigma_b^2}\right\}\sin\left\{\frac{2\pi(x-x_b)}{l_b}\right\}, \quad (26)$$

where l_b is the length of the slot, x_b is the center of the slot measured from the leading edge of the cone, ϵ_b scales the function, μ_b shifts the Gaussian component to avoid negative times, and σ_b adjusts the spectral content of the function. Notice the time dependent Gaussian portion of the function. When transformed to frequency space, this yields a continuous range of frequencies with non-zero amplitudes making this particular approach for perturbing the mean flow an effective strategy when studying a wide range of frequencies. Alternatively, a sinusoid in time can be used to similar effect.[20,21]

The pulse parameters for both cases are summarized in Table II. The frequency spectrum of the pulse is presented in Fig. 8. The Fourier transform indicates that the majority of the frequency content of the pulse is below 1 MHz. From the LST analysis, it was predicted that the unstable modes leading to transition will be present below this frequency. The amplitude of the perturbation is small enough that the disturbance is approximately linear.

A. Case 1 unsteady DNS results

The evolution of the Gaussian pulse for Case 1 is visualized in Fig. 9 using snapshots in time of contours of the pressure perturbation normalized by the local meanflow pressure ($\frac{\Delta p}{p}$). The same value at the surface of the cone is included to more clearly visualize the growth of disturbances. The traditional second mode growth can be seen in Fig. 9(a), in particular, between x = 0.3 m and x = 0.45 m. The start of the spontaneous radiation of sound appears in Fig. 9(b) between x = 0.35 m and x = 0.4 m. When the pulse travels to approximately x = 0.5 m, the spontaneous radiation of sound becomes much more apparent, shown in Fig. 9(c). As the pulse continues downstream, the supersonic mode elongates farther into the free steam before decaying in amplitude far away from the wall. Simultaneously, the amplitude of the disturbance outside of the boundary layer increases as the pulse travels downstream [Fig. 9(d)]. The perturbations near the upper boundary in Figs. 9(a) and 9(b) are a result of the Mach wave from the pulse traveling downstream and eventually interacting with

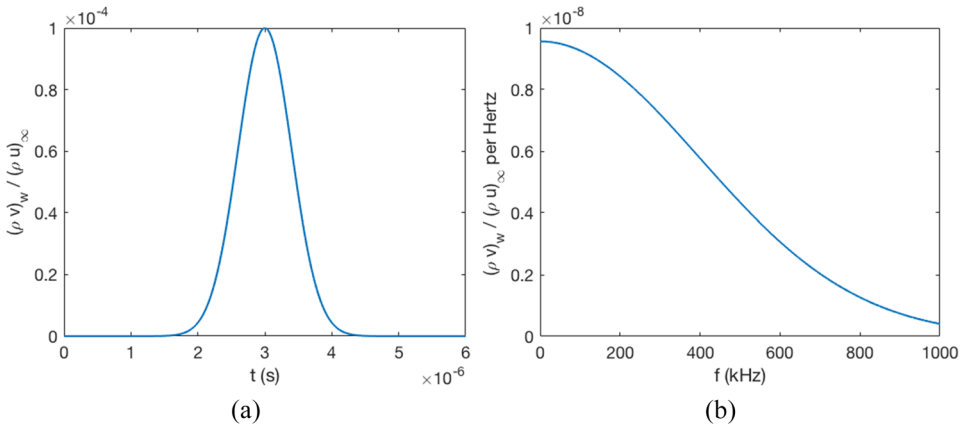

FIG. 8. Gaussian pulse for unsteady DNS. (a) Nondimensional mass flux amplitude. (b) Frequency content of pulse.

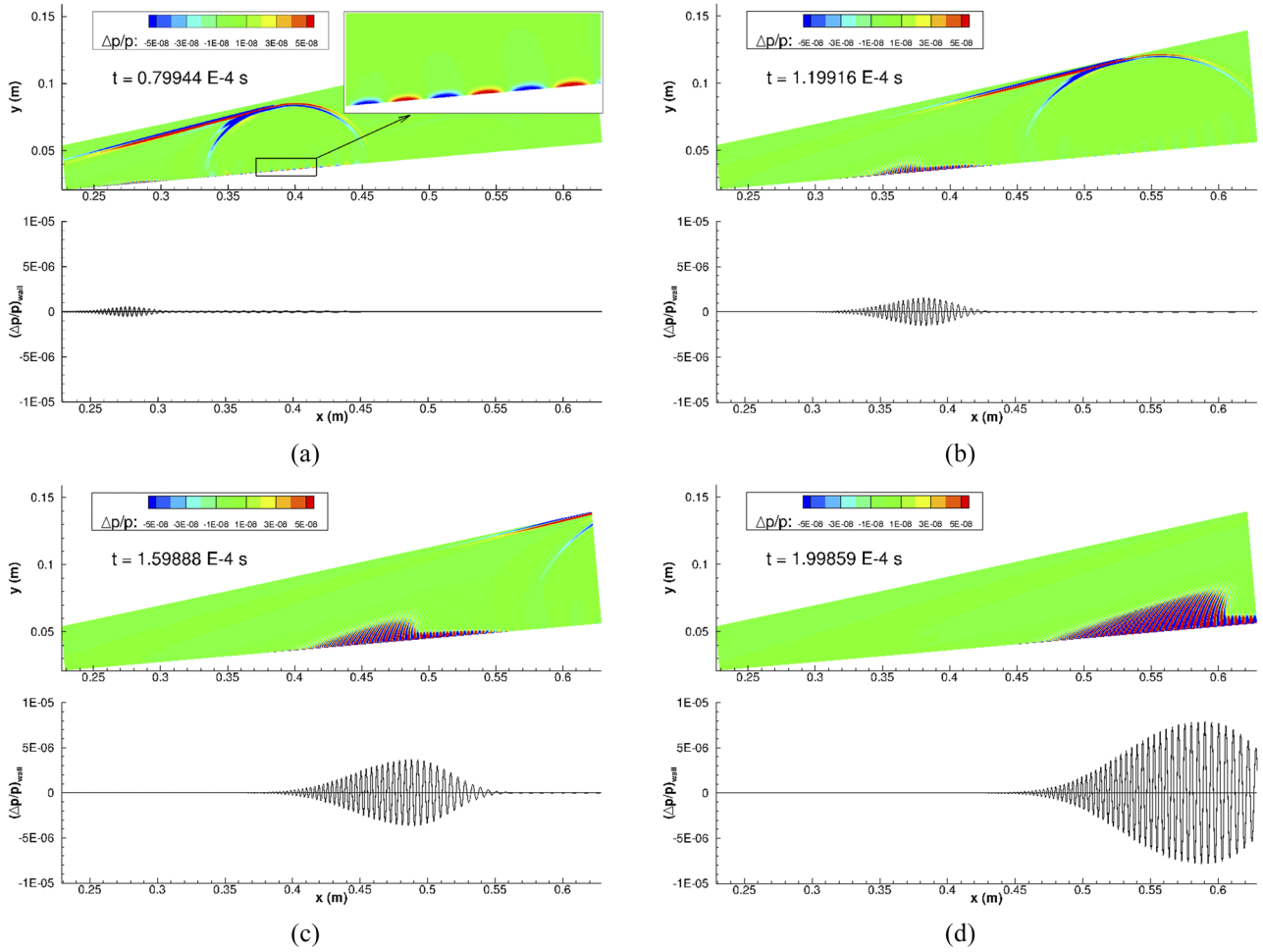

FIG. 9. Case 1 snapshots in time of pressure perturbation $\Delta p/p$ contours and surface pressure perturbation from Gaussian pulse. $\Delta t = 3.997 \times 10^{-5}$ s.

the shock. These interactions are weak, however, and disperse before the spontaneous radiation of sound occurs.

An FFT was performed for the surface pressure perturbation at all streamwise locations, resulting in the contour map in Fig. 10(a). This contour shows the most unstable excited frequencies due to the Gaussian pulse. The neutral stability curve predicted by LST is overlayed in Fig. 10(a) for comparison. The most amplified frequency is approximately f = 500 kHz and appears most prominently for $s >$ 0.9 m. This frequency agrees with the largest N-factor (see Paper I[72]), and the location of the maximum amplification agrees reasonably well with the LST predictions, i.e., the upper branch of the neutral curve coincides with the location of largest amplification for each frequency.

It is useful to compare the FFT results to those obtained by Chuvakhov and Fedorov,[20,21] although their unsteady DNS perturbs the flow with a sinusoidal pulse in time, rather than the Gaussian pulse that is used here. Nevertheless, this difference is unlikely to be significant because the band of frequencies excited by the sinusoid is large. Chuvakhov and Fedorov[20,21] take a Fourier transform of the unsteady data and present the FFT of the pressure perturbation vs the frequency for fixed streamwise locations. An example of such a figure for the current investigation is shown in Fig. 10(b), where the curve shape is similar to a bell curve. Chuvakhov and Fedorov[20,21] noted that rather than the typical bell-shaped curves, multiple peaks are formed. Chuvakhov and Fedorov[20,21] observed three peaks at most in their FFT, which may have been due to the significantly differing geometry and flow conditions from the current study. The same authors have suggested that the mechanism of sound radiation acts as an energy sink, which may explain the abnormal behavior of the pulse dispersion. Furthermore, Chuvakhov and Fedorov[20,21] suggest that the spontaneous radiation of

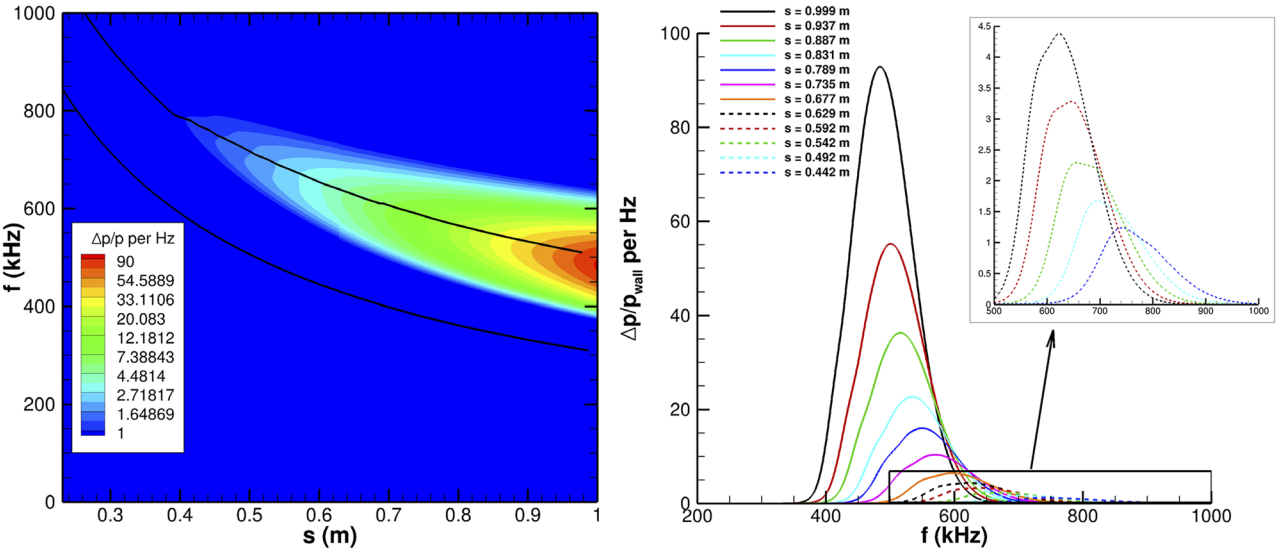

FIG. 10. Case 1 Fourier transform of unsteady surface pressure perturbation time history of Gaussian pulse. (a) FFT stability map with LST neutral curve. (b) FFT amplitude as a function of frequency for various streamwise locations *s*.

sound is a mechanism that transfers the disturbance energy from the high-frequency to the low-frequency band. Further detailed investigation into this phenomenon is required to ascertain the mechanism by which the spontaneous radiation of sound modulates the surface pressure perturbation and whether or not the frequency content of the disturbance plays a significant role in the spontaneous radiation of sound.

It is possible to determine the growth rate and phase speed of an unsteady disturbance in DNS. The Fourier decomposed perturbation variables can be used to reconstruct the original flow field disturbances via

$$\phi'(x,y,t) = \Delta\phi(x,y)\exp[i(\psi(x,y) - 2\pi f t)], \tag{27}$$

where ϕ' is the perturbation of some variable, $\Delta\phi$ is the amplitude of that variable, ψ is the corresponding phase angle, and f represents a single dimensional frequency. An instantaneous snapshot of the flow field can be obtained from the real part of ϕ' when t is specified, provided FFT data is available for all data points in the flow field.

Multiple boundary layer modes are present simultaneously in DNS; however, as one mode becomes dominant, it is possible to derive the growth rate, wavenumber, and phase speed equations for a given frequency f from [Eq. (27)], resulting in

$$-\alpha_i = \frac{1}{\Delta\phi(f)}\frac{d}{ds}\Delta\phi(f), \tag{28}$$

$$\alpha_r = \frac{d}{ds}\psi(f), \tag{29}$$

$$c_r = \frac{2\pi f}{\alpha_r}, \tag{30}$$

where s is the streamwise coordinate, $\Delta\phi(f)$ represents a variable amplitude frequency f, and $\psi(f)$ represents the corresponding phase angle at frequency f. Similar to previous researchers,[13] the surface pressure perturbations from DNS are used to compute $-\alpha_i$ and c_r.

The frequency f = 500 kHz was chosen to compare the phase speed and growth rate obtained from DNS to those predicted by LST (Fig. 11). The phase speed calculated from DNS matches the LST predictions quite well, with the exception of oscillations near s = 0.5 m. These oscillations are the result of the synchronization of mode F1 with mode S and with the entropy/vorticity spectra. The DNS growth rate exhibits much more oscillatory behavior, although it still follows the LST prediction reasonably well. The DNS growth rate oscillations can be attributed to multiple modes existing in the flow; however, the overall amplitude of the DNS growth rate can be impacted by nonparallel flow effects neglected in LST. Interestingly, the DNS growth rate also displays the "kink" which indicates synchronization of the mode F1$^+$ with the slow acoustic spectrum, leading to the spontaneous radiation of sound. However, this kink appears slightly farther downstream for DNS than for LST and may be due to nonparallel flow effects. The LST growth rate kink occurs near s = 0.75 m, whereas the DNS kink occurs near s = 0.79 m.

In the region in which mode F1$^+$ is dominant in the flow, the DNS most closely follows the LST predictions. Areas where the DNS growth rate is oscillatory suggest the

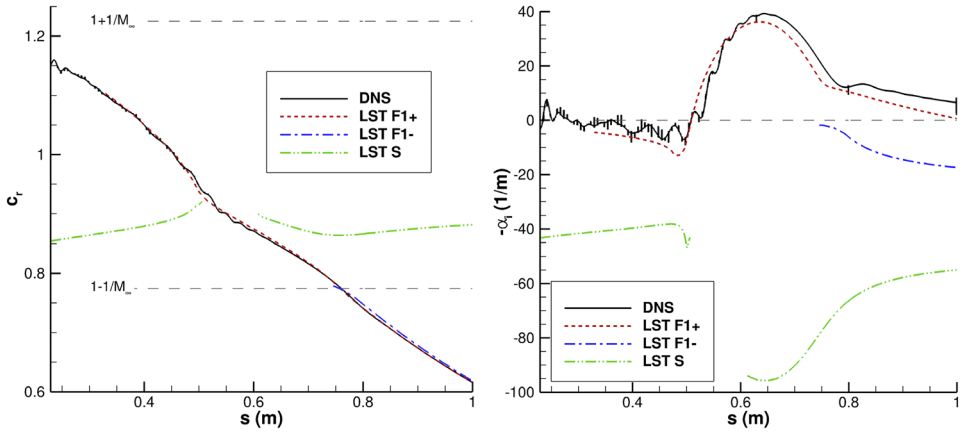

FIG. 11. Case 1 comparison of DNS to LST phase speed and growth rate at f = 500 kHz. (a) Phase speed, c_r. (b) Growth rate, $-\alpha_i$. M_∞ = 4.44 is the mean flow Mach number immediately downstream of the shock.

presence of multiple modes in the flow in addition to the amplitude discrepancy caused by nonparallel flow effects. The pressure eigenfunctions from DNS at a frequency of f = 500 kHz are compared to those from LST at three locations. The first is at s = 0.7 m where mode $F1^+$ is unstable and subsonic, as shown in Fig. 12(a). The second is at s = 0.8 m where mode $F1^+$ is unstable and supersonic and mode $F1^-$ is stable and supersonic, as shown in Fig. 12(b). The third is at s = 0.9 m

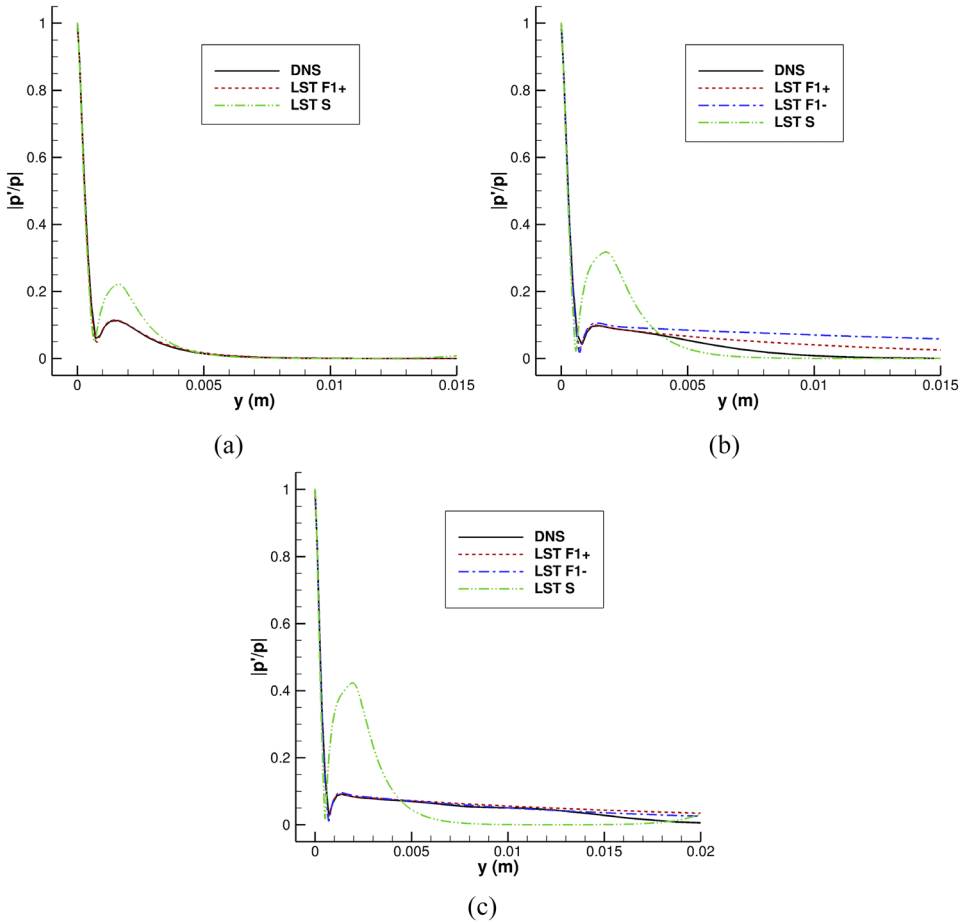

FIG. 12. Case 1 comparison of DNS to LST pressure eigenfunctions at f = 500 kHz. (a) Subsonic mode $F1^+$ at s = 0.7 m. (b) Supersonic mode $F1^+$ at s = 0.8 m. (c) Supersonic mode $F1^+$ at s = 0.9 m.

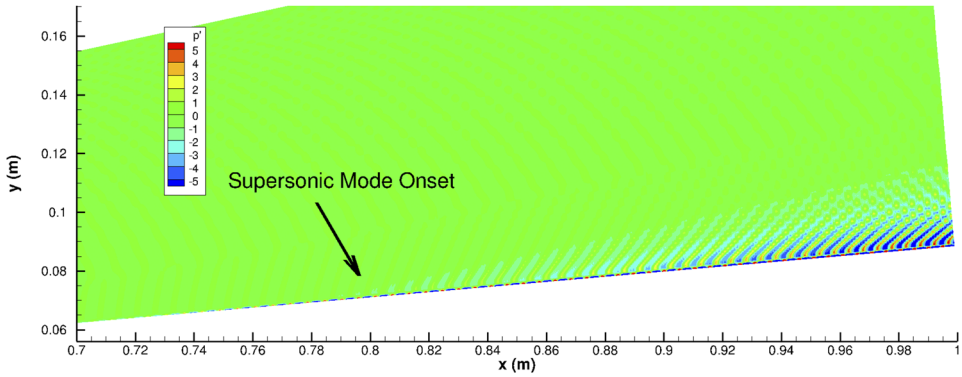

FIG. 13. Case 1 Fourier transform of unsteady pressure perturbation field for f = 500 kHz.

where mode F1$^+$ is unstable and supersonic and mode F1$^-$ is stable and supersonic, as shown in Fig. 12(c). The DNS eigenfunction at s = 0.7 m [Fig. 12(a)] matches the LST mode F1$^+$ eigenfunction nearly identically, indicating the dominance of the unstable subsonic mode F1$^+$ in this location. At s = 0.8 m [Fig. 12(b)], the DNS eigenfunction matches the LST mode F1$^+$ predictions near the wall for $y < 0.004$ m, although the DNS eigenfunction decays to zero more sharply than the LST eigenfunction, indicating that the supersonic mode F1$^+$ from LST may not be the only factor in the supersonic mode found in DNS. It is possible that the slow acoustic spectrum is still interacting with mode F1$^+$ which is not accounted for in LST. It should be noted that the eigenfunction of mode F1$^-$ is similar to mode F1$^+$ and the DNS eigenfunctions; however, the mode F1$^-$ eigenfunction does not decay as rapidly and mode F1$^+$ still appears to have the greatest similarity to the DNS perturbation. Furthermore, because the DNS growth rate is predicted to be unstable (Fig. 11), it suggests better agreement with LST mode F1$^+$. Additionally, it appears that mode S does not make up a large component of the DNS perturbation at this location. Farther downstream at s = 0.9 m [Fig. 12(c)], the DNS, LST mode F1$^+$, and LST mode F1$^-$ eigenfunctions match closely for $y < 0.014$ m, outside of which the DNS eigenfunction decays more sharply than the LST eigenfunctions. The LST mode F1$^+$ and F1$^-$ eigenfunctions are nearly identical; however, due to the LST mode F1$^+$ and DNS growth rates being unstable, it is likely that mode F1$^+$ is still the dominant mode as opposed to mode F1$^-$. Additionally, because this location is farther removed from the synchronization of mode F1$^+$ with the slow acoustic spectrum, its influence is smaller than at s = 0.8 m. Again, mode S does not appear to constitute a significant portion of the DNS perturbation at this location. Nevertheless, the deviation of the DNS eigenfunction from the LST prediction suggests that the slow acoustic spectrum may still be modulating the disturbance.

The FFT of the pressure perturbation for the entire flow field was calculated via Eq. (27) and is shown in Fig. 13 for 500 kHz, which clearly shows the extension of the disturbance outside of the boundary layer, indicative of the supersonic mode. The onset of the radiation into the free stream for f = 500 kHz is near x = 0.8 m, as indicated by the arrow in Fig. 13. The onset of the supersonic mode in this 2D FFT contour agrees with the LST and FFT results for the surface pressure perturbation in Fig. 11. However, the magnitude of the surface pressure perturbation is significantly higher than the

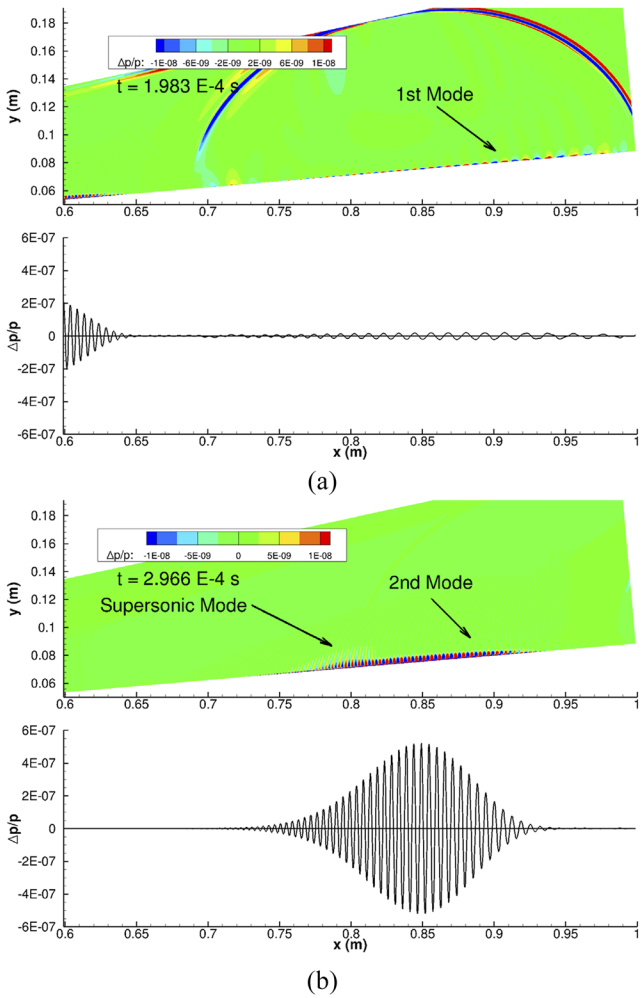

FIG. 14. Case 2 snapshots in time of pressure perturbation $\Delta p/p$ contours and surface pressure perturbation from Gaussian pulse. $\Delta t = 9.83 \times 10^{-5}$ s.

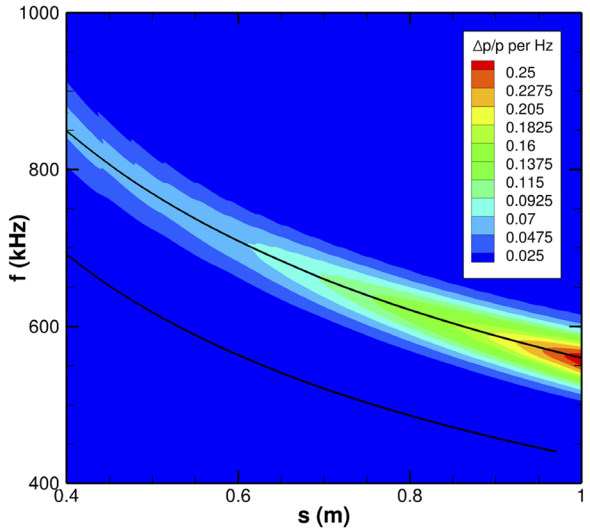

FIG. 15. Case 2 Fourier transform of unsteady surface pressure perturbation time history of Gaussian pulse. The black line is the neutral curve predicted by LST.

amplitude of the supersonic mode. Therefore, it is unlikely that the supersonic mode will directly lead to transition in this flow configuration. That being said, however, because the supersonic mode radiates energy away from the boundary layer, its impact on the boundary layer disturbance is unclear. It may be possible that the boundary layer disturbance can be weakened by the radiation of sound by dispersing some of its energy into the free stream, effectively stabilizing mode $F1^{+}$. Alternatively, it is also possible for the elongation of the unstable region due to the supersonic mode to lead to a larger overall N-factor, thereby causing transition earlier on the body. Significant theoretical work must be performed to fully understand the mechanism of the supersonic mode and its impact on transition to turbulence in hypersonic boundary layers.

B. Case 2 unsteady results

The unsteady pressure perturbation due to the Gaussian pulse for Case 2 was not expected to produce a significant supersonic mode. However, there is a very clear "tail" that develops downstream, which is indicative of the supersonic mode. Snapshots of the unsteady pressure perturbation are shown in Fig. 14 which shows the weaker first mode disturbance leading stronger second mode disturbance in Fig. 14(a). Additionally, in Fig. 14(b), the second mode disturbance can be seen ahead of the supersonic mode "tail" extending into the free stream. This extension into the free stream is significantly weaker than in Case 1, but may not be negligible. Further FFT analysis is performed to determine the cause of the supersonic mode encountered in Fig. 14.

A FFT was performed for the surface pressure perturbation at all streamwise locations, resulting in the contour map in Fig. 15 with the neutral stability curve predicted by LST overlayed for comparison. The most amplified frequency is approximately f = 550 kHz and appears most prominently for $s > 0.95$ m. This frequency agrees with the largest N-factor (see Paper I[72]), and the location of the maximum amplification agrees reasonably well with the LST predictions, i.e., the upper branch of the neutral curve coincides with the location of largest amplification for each frequency.

The FFT contour in Fig. 15 provides good agreement between LST and DNS but does not explain the "tail" of the supersonic mode in Fig. 14. The phase speed and growth rate obtained from DNS, computed via Eqs. (28)–(30), is compared to the LST results for a frequency of f = 700 kHz in Fig. 16. The DNS phase speed most closely follows LST mode F1 upstream of s = 0.75 m; however, there are very significant oscillations near the synchronization with the entropy/vorticity spectra and the slow acoustic spectrum. The oscillations in the DNS results are the influence of multiple modes in the flow, whereas LST only assumes a single mode at a time and neglects the interactions between modes. The growth rate upstream of s = 0.75 m also largely follows mode F1 with some oscillations. After synchronization with the slow

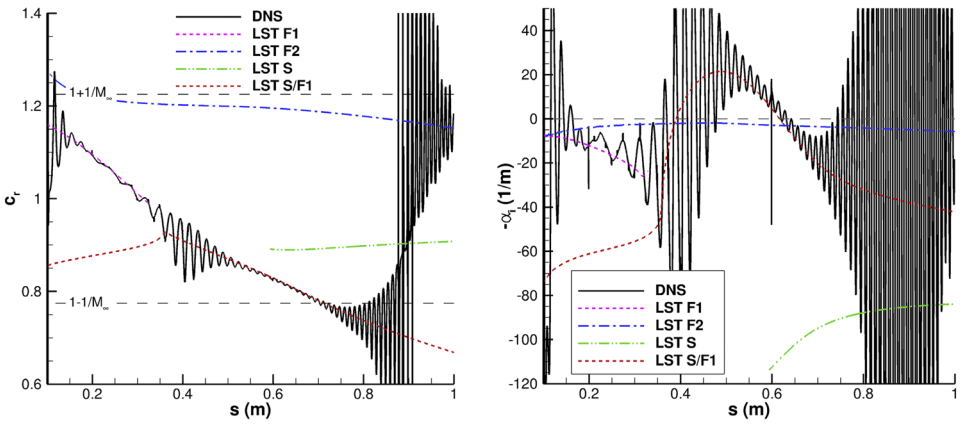

FIG. 16. Case 2 comparison of DNS to LST phase speed and growth rate at f = 700 kHz. (a) Phase speed, c_r. (b) Growth rate, $-\alpha_i$. M_∞ = 4.44 is the mean flow Mach number immediately downstream of the shock.

acoustic spectrum near s = 0.75 m, however, very large oscillations in both the phase speed and growth rate occur. These oscillations signify a strong resonant interaction between the unstable mode F1 and the slow acoustic spectrum that is not resolved with LST. After this synchronization, the DNS phase speed appears to be following mode F2 more closely.

The eigenfunction of the pressure disturbance from DNS is compared to LST in two locations for the same fixed frequency of f = 700 kHz. The first is in the region where the DNS phase speed and growth rates most closely follow the LST predictions, indicating the dominance of mode F1. This occurs at s = 0.617 m and is shown in Fig. 17(a). The second is in the region where the mode F1 phase speed is supersonic and the mode is stable according to LST, occuring at s = 0.8 m [Fig. 17(b)]. Where mode F1 is dominant [Fig. 17(a)], the DNS pressure eigenfunction is nearly exact to the LST mode F1 predictions, indicating a good agreement between the methods in describing the boundary layer instabilities despite the difference in techniques. However, in the region where mode F1 is predicted to be supersonic and stable by LST [Fig. 17(b)], the agreement is not as strong, suggesting the presence of multiple competing modes. Very near the wall, the pressure eigenfunctions align between DNS and all of the LST eigenfunctions; however, for $y > 0.001$ m, the eigenfunctions are significantly different. The local maximum in the LST mode F1 eigenfunction occurs near $y \approx 0.0015$ m and has a magnitude of $|p'/p| \approx 0.1$, whereas the DNS eigenfunction's local maximum occurs much farther away from the wall at $y \approx 0.0075$ m and shows a significantly larger amplitude of $|p'/p| \approx 0.3$. Additionally, the LST mode S and F2 eigenfunctions do not provide any better agreement. The local maximum in the eigenfunction moving outwards is indicative of an unstable supersonic mode, whereas LST predicts the supersonic mode F1 and all other subsonic modes to be stable in this location. Therefore, at this location of s = 0.8 m, the LST predictions no longer accurately describe the dominant instability in the flow field. Rather, the DNS eigenfunction in conjunction with the phase speed and growth rate results in Fig. 16 suggest the excitation of the supersonic mode via a modal interaction that cannot be resolved with LST.

The supersonic mode is known to exist downstream to the synchronization of mode F1 with the slow acoustic spectrum. Figure 16 shows that this synchronization occurred near s = 0.75 m and produced significant amplification of the growth rate of the surface pressure perturbation that was not predicted by LST. This notion was also supported by the eigenfunction comparison in Fig. 17. To determine if this resonant interaction produced the supersonic mode "tail" in Fig. 14, an FFT of the entire unsteady flow field was performed for a frequency of f = 700 kHz (Fig. 18). The Mach waves from the original perturbation are visible in the free stream and the dominant second mode growth is clear in Fig. 18 for $x <$ 0.75 m. Downstream of x = 0.75 m, however, there is a clear extension of the disturbance into the free stream, indicative of the supersonic mode. The onset of this extension coincides precisely with the synchronization of the stable mode F1 with the slow acoustic continuous spectrum. Although all LST modes are predicted to be stable at this location, it is the interaction between modes in DNS that causes this very brief supersonic instability, and therefore it is not resolved with LST. Ma and Zhong[13,66,67] note an interaction between the discrete mode F1 and the continuous slow acoustic spectrum can act as a source term in the stability equations, which briefly causes mode F1 to become unstable when its phase speed is supersonic ($c_r < 1 - 1/M_\infty$). Most importantly, however, the amplitude of the supersonic mode is two orders of magnitude lower than the second mode and is very unlikely to have any significant impact on transition to turbulence.

Modal interactions have been examined in a number of circumstances. In addition to Ma and Zhong[13,66,67] commenting on the interaction of mode F1 with the fast acoustic spectrum, studies by Fedorov and Khokhlov,[68,69] Fedorov,[70] Gushchin and Fedorov,[71] and later by Fedorov and Tumin[2] examine the synchronization of discrete modes with continuous modes. In general, theoretical studies have shown that the synchronization of a discrete mode with a continuous

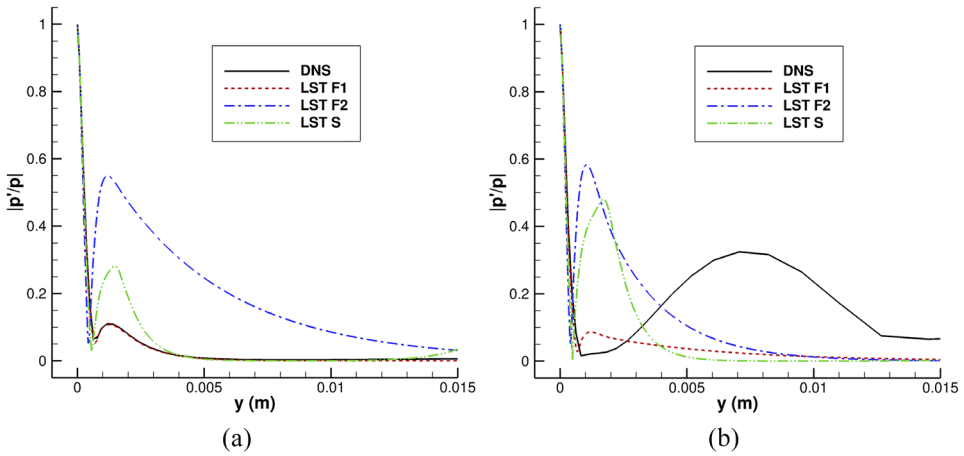

FIG. 17. Case 2 comparison of DNS to LST pressure eigenfunctions at f = 700 kHz. (a) Dominant subsonic unstable mode F1 region at s = 0.617 m. (b) Supersonic, stable mode F1 region at s = 0.8 m.

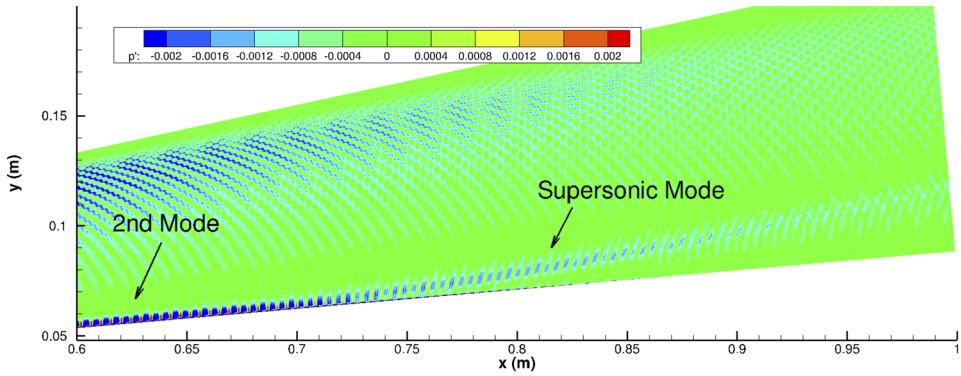

FIG. 18. Case 2 Fourier transform of unsteady pressure perturbation field for f = 700 kHz. Contour levels adjusted to show weak supersonic mode.

mode can cause oscillatory behavior in the free stream, similar to the supersonic mode. However, a theoretical investigation of the supersonic mode mechanism specifically is yet to be performed.

VII. DISCUSSION OF RESULTS AND CONCLUSION

Thermochemical nonequilibrium LST and DNS were used to study the supersonic mode and its impact on hypersonic boundary layer transition in Mach 5 cold-wall conical flow. Additionally, the effect of wall temperature on stability was examined; Case 1 used a wall-temperature-ratio of T_w/T_∞ = 0.2 and Case 2 used T_w/T_∞ = 0.667. The steady flow fields for both Case 1 and Case 2 showed strong thermochemical nonequilibrium effects in the nose region; however, the chemical nonequilibrium effects became less significant farther downstream. A surface blow/suction actuator on the cone upstream of the region of eigenmode growth was used to perturb the mean flow and examine the growth and decay of the disturbance. LST was used to estimate the region of eigenmode growth and identify the expected modes leading to transition to turbulence; however, LST makes the limiting assumption of each mode acting independently. LST predictions indicated the unstable supersonic mode in Case 1, but no unstable supersonic mode was expected in Case 2 according to LST. However, in addition to confirming the Case 1 LST predictions validating the existence of the supersonic mode, the DNS results actually suggested a weakly unstable supersonic mode in Case 2 that could not be resolved in LST due to modal interactions, demonstrating the need for a combined LST and DNS approach to studying the supersonic mode.

The unstable supersonic mode was shown to exist on an axisymmetric cone through both LST and unsteady DNS analysis for Case 1 (T_w/T_∞ = 0.2). However, only DNS was able to resolve a very weak unstable supersonic mode for Case 2 (T_w/T_∞ = 0.667) due to the interaction of the stable supersonic mode F1 with the slow acoustic spectrum. The relative modal composition of the DNS perturbation was estimated via comparison to the LST phase speed, growth rate, and eigenfunctions. When a single mode is dominant, the agreement between LST and DNS was excellent. However when no single mode was dominant, the agreement was not as strong and oscillations in the growth rate indicated multiple competing modes in the DNS. Furthermore, nonparallel flow effects could have led to a difference in the amplitude of the growth rate in DNS compared to LST. The resonant interaction leading to the supersonic mode in Case 2 was due to the synchronization of mode F1 and the slow acoustic spectrum and acted as a source term in the LST equations,[13,66,67] which were neglected in the current LST formulation.

These findings on an axisymmetric blunt cone with thermochemical nonequilibrium effects reinforce the results obtained for the flat plate geometry by Bitter and Shepherd[15] and Chuvakhov and Fedorov,[20,21] indicating that the cold wall is destabilizing to the supersonic mode. The formation of the unstable supersonic modes is only predicted by LST for an individual frequency as a peculiarity of the spectrum in the vicinity of synchronization of the unstable discrete boundary layer mode F1 and the continuous slow acoustic spectrum. Such was the mechanism of the supersonic mode in Case 1. If mode F1 is stable upon synchronization with the slow acoustic spectrum, however, a resonant interaction between modes can cause mode F1 to become unstable briefly. Such was the mechanism of the supersonic mode determined in Case 2; however, it did not have a significant impact on the boundary layer stability. As Knisely and Zhong[47,48] have shown, this resonant interaction can become significant in higher-enthalpy flow, however.

The unsteady DNS results confirmed that the supersonic mode existed at the same location as predicted by LST results for Case 1. Both the wall pressure perturbation FFT and the full 2D FFT contour reinforced the LST predictions of the onset and magnitude of the supersonic mode. The unstable frequencies predicted by the LST analysis corresponded to the most amplified frequencies in the unsteady DNS results. The major finding from the FFT results of the unsteady DNS pressure pulse contradicts the multiple peak frequencies observed by Chuvakhov and Fedorov.[20,21] Rather than certain frequencies being more amplified than their neighboring frequencies, the typical bell-shaped curves were obtained for the pressure perturbation as a function of frequency for a fixed location. The mechanism by which the acoustic radiation modulates the

pressure disturbance is not yet well understood, and further studies are required to fully describe this abnormal behavior and determine the influence of the frequency content of the disturbance on the supersonic mode.

Overall, the present results show that the radiation of sound by the supersonic mode is the result of the complex interaction of a number of physical modes. The interaction of the acoustic waves with the boundary layer disturbance is of significance because it could play a role in energy transfer to the vehicle surface and could have an impact on boundary layer stability, as suggested by Chuvakhov and Fedorov.[20,21] Specifically, the relatively weak supersonic mode may act as an energy sink for the second mode by radiating energy away from the boundary layer and may have a stabilizing effect on the boundary layer mode. However, the supersonic mode is also associated with a longer region of instability, which may have the opposite effect of causing transition earlier on the cone. The work performed here is not conclusive in regards to the stabilizing/destabilizing effect of the supersonic mode. Additionally, it is unclear under which conditions the supersonic mode could become the dominant transition mechanism over the second mode. Thus far, only Knisely and Zhong[48] and Mortensen[49] have encountered such a situation on a Mach 10 cold-wall blunt cone and on a Mach 20 very blunt cone, respectively. Further research is required to determine the envelope of conditions for such a strong supersonic mode.

The work performed here has confirmed the existence of the supersonic mode using a combined LST and DNS approach and shows some of its overarching characteristics. Thus far, only the present work, that of Knisely and Zhong,[47,48,50] Mortensen,[49] and Chuvakhov and Fedorov,[20,21] have studied the supersonic mode using a combined LST and DNS approach. The supersonic mode has been shown to be destabilized by a cold wall, as suggested by Bitter and Shepherd[15] and Chuvakhov and Fedorov.[20,21] The mechanism of the supersonic mode, however, may have been limited in previous pure LST studies and not fully described by Mortensen[49] and Chuvakhov and Fedorov.[20,21] Both LST and DNS can agree that the supersonic mode is encountered downstream of the synchronization of mode F1 with the slow acoustic spectrum. However, LST is not able to resolve the supersonic mode in certain cases due to the assumption of independent modes. Only when mode F1 is unstable during synchronization with the slow acoustic spectrum will LST accurately predict the supersonic mode. When mode F1 is stable during synchronization, a resonant-like interaction between mode F1, mode S, and the slow acoustic spectrum can cause a brief excitation of the supersonic mode, which is not resolved in LST. Therefore, a combined LST and DNS study is required to reliably resolve the supersonic mode and study its impact on transition to turbulence.

ACKNOWLEDGMENTS

This research was supported by the U.S. Air Force Office of Scientific Research (AFOSR) through the National Defense Science and Engineering Graduate Fellowship (NDSEG) Program. This research was also partially supported by the AFOSR, USAF, under AFOSR Grant No. FA9550-15-1-0268, monitored by Dr. Ivett Leyva, and by the Office of Naval Research (ONR) Grant No. N00014-17-1-2343, monitored by Dr. Eric Marineau currently and by Dr. Knox Millsaps previously. Primary computational resources were provided by the AFOSR with additional computational resources provided by Extreme Science and Engineering Discovery Environment (XSEDE) through Texas Advanced Computing Center (TACC) and San Diego Supercomputer Center (SDSC) under Grant No. TG-ASC090076, supported in part by the National Science Foundation. The views and conclusions contained herein are those of the authors and should not be interpreted as necessarily representing the official policies or endorsements, either expressed or implied, of the U.S. Air Force Office of Scientific Research, Office of Naval Research, or the U.S. Government.

REFERENCES

[1] L. M. Mack, "Boundary layer linear stability theory," AGARD Report No. 709, 1984.
[2] A. Fedorov and A. Tumin, "High-speed boundary-layer instability: Old terminology and a new framework," AIAA J. **49**, 1647–1657 (2011).
[3] M. V. Morkovin, "Transition at hypersonic speeds," ICASE Interim Report 1, NASA Contractor Report 178315, ICASE, NASA Langley Research Center, Hampton, VA 23665, 1987.
[4] L. M. Mack, "On the inviscid acoustic-mode instability of supersonic shear flows. I. Two-dimensional waves," Theor. Comput. Fluid Dyn. **2**, 97–123 (1990).
[5] E. Reshotko, "Hypersonic stability and transition," *Hypersonic Flows for Reentry Problems* (Springer-Verlag, Berlin, 1991), Vol. 1, pp. 18–34.
[6] A. Fedorov, "Transition and stability of high-speed boundary layers," Annu. Rev. Fluid Mech. **43**, 79–95 (2011).
[7] V. Gushchin and A. Fedorov, "Asymptotic analysis of inviscid perturbations in a supersonic boundary layer," J. Appl. Mech. Tech. Phys. **30**, 64–70 (1989).
[8] A. Demetriades, "Hypersonic viscous flow over a slender cone. III. Laminar instability and transition," AIAA Paper No. 74-535, 1974.
[9] C.-H. Zhang, Q. Tang, and C.-B. Lee, "Hypersonic boundary-layer transition on a flared cone," Acta Mech. Sin. **29**, 48–54 (2013).
[10] X. Zhong and Y. Ma, "Boundary-layer receptivity of Mach 7.99 flow over a blunt cone to free-stream acoustic waves," J. Fluid Mech. **556**, 55–103 (2006).
[11] N. Parsons, X. Zhong, J. Kim, and J. Eldredge, "Numerical study of hypersonic receptivity with thermochemical non-equilibrium on a blunt cone," AIAA Paper 2010-4446, 2010.
[12] D. Heitmann and R. Radespiel, "Simulation of the interaction of a laser generated shock wave with a hypersonic conical boundary layer," AIAA Paper 2011-3875, 2011.
[13] Y. Ma and X. Zhong, "Receptivity of a supersonic boundary layer over a flat plate. I. Wave structures and interactions," J. Fluid Mech. **488**, 31–78 (2003).
[14] L. Mack, "Review of linear compressible stability theory," in *Stability of Time Dependent and Spatially Varying Flows*, edited by D. Dwoyer and M. Hussaini (Springer-Verlag, 1985), pp. 164–187.
[15] N. Bitter and J. Shepherd, "Stability of highly cooled hypervelocity boundary layers," J. Fluid Mech. **778**, 586–620 (2015).
[16] M. M. Sherman and T. Nakamura, "Flight test measurements of boundary-layer transition on a nonablating 22 deg cone," J. Spacecr. Rockets **7**, 137–142 (1970).
[17] M. R. Malik, "Hypersonic flight transition data analysis using parabolized stability equations with chemistry effects," J. Spacecr. Rockets **40**, 332–344 (2003).

[18]L. Lees, "The stability of the laminar boundary layer in a compressible fluid," Technical Report 876, NACA, 1947.
[19]L. Mack, "Effect of cooling on boundary-layer stability at Mach number 3," in *Instabilities and Turbulence in Engineering Flows*, edited by D. Ashpis, T. Gatski, and R. Hirsch (Springer-Verlag, 1993).
[20]P. Chuvakhov and A. Fedorov, "Spontaneous radiation of sound by instability of a highly cooled hypersonic boundary layer," in 8th AIAA Flow Control Conference, 2016.
[21]P. Chuvakhov and A. Fedorov, "Spontaneous radiation of sound by instability of a highly cooled hypersonic boundary layer," J. Fluid Mech. **805**, 188–206 (2016).
[22]A. Fedorov, G. Bres, M. Inkman, and T. Colonius, "Instability of hypersonic boundary layer on a wall with resonating micro-cavities," in 49th AIAA Aerospace Sciences Meeting, 2011.
[23]R. Wagnild, "High enthalpy effects on two boundary layer disturbances in supersonic and hypersonic flow," Ph.D. thesis, University of Minnesota, Minneapolis, MN, 2012.
[24]G. Bres, M. Inkman, T. Colonius, and A. Fedorov, "Second-mode attenuation and cancellation by porous coatings in a high-speed boundary layer," J. Fluid Mech. **726**, 312–337 (2013).
[25]J. Klentzman and A. Tumin, "Stability and receptivity of high speed boundary layers in oxygen," AIAA Paper 2013-2882, 2013.
[26]J. Jewell, "Boundary-layer transition on a slender cone in hypervelocity flow with real gas effects," Ph.D. thesis, California Institute of Technology, 2014.
[27]A. Fedorov, V. Soudakov, and I. Leyva, "Stability analysis of high-speed boundary-layer flow with gas injection," in 7th AIAA Theoretical Fluid Mechanics Conference, 2014.
[28]A. Sescu, J. Sawaya, V. Sassanis, and M. Visbal, "Study of the effect of two-dimensional wall non-uniformities on high-speed boundary layers," AIAA Paper 2017-4511, 2017.
[29]G. Candler, "The computation of weakly ionized hypersonic flows in thermochemical nonequilibrium," Ph.D. thesis, Stanford University, 1988.
[30]I. Nompelis, T. Drayna, and G. Candler, "Development of a hybrid unstructured implicit solver for the simulation of reacting flows over complex geometries," AIAA Paper 2004-2227, 2004.
[31]F. Cheatwood and P. Gnoffo, "Users manual for the Langley aerothermal upwind relaxation algorithm (LAURA)," Report No. NASA TM-4674, 1996.
[32]P. Gnoffo, R. Gupta, and J. Shinn, "Conservation equations and physical models for hypersonic air flows in thermal and chemical nonequilibrium," Report No. NASA TP-2867, 1989.
[33]M. Wright, G. Candler, and D. Bose, "Data-parallel line relaxation method for the Navier-Stokes equations," AIAA J. **36**, 1603–1609 (1998).
[34]C. Stemmer, "Transition investigation on hypersonic flat-plate boundary layers flows with chemical and thermal non-equilibrium," in *Sixth IUTAM Symposium on Laminar-Turbulent Transition*, Fluid Mechanics and Its Applications Vol. 78 (Springer, Dordrecht, 2006), pp. 363–368.
[35]C. Stemmer, "Instability of high Mach number flows in the presence of high-temperature gas effects," in *Seventh IUTAM Symposium on Laminar-Turbulent Transition*, IUTAM Bookseries Vol. 18 (Springer, Dordrecht, 2009), pp. 391–396.
[36]J. Linn and M. Kloker, "Investigation of thermal nonequilibrium on hypersonic boundary-layer transition by DNS," in *Seventh IUTAM Symposium on Laminar-Turbulent Transition*, IUTAM Bookseries Vol. 18 (Springer, Dordrecht, 2009), pp. 521–524.
[37]Y. Ma and X. Zhong, "Receptivity to freestream disturbances of a Mach 10 nonequilibrium reacting oxygen flow over a flat plate," AIAA Paper 2004-0256, 2004.
[38]A. Prakash, N. Parsons, X. Wang, and X. Zhong, "High-order shock-fitting methods for direct numerical simulation of hypersonic flow with chemical and thermal nonequilibrium," J. Comput. Phys. **230**, 8474–8507 (2011).
[39]C. H. Mortensen, "Effects of thermochemical nonequilibrium on hypersonic boundary-layer instability in the presence of surface ablation and isolated two-dimensional roughness," Ph.D. thesis, University of California Los Angeles, 2015.
[40]C.-L. Chang, H. Vinh, and M. Malik, "Hypersonic boundary-layer stability with chemical reactions using PSE," in 28th AIAA Fluid Dynamics Conference, Snowmass Village, CO, USA, 1997.
[41]L. Salemi, H. Fasel, S. Wernz, and E. Marquart, "Numerical investigation of wave-packets in a hypersonic high-enthalpy boundary-layer on a 5 degree sharp cone," in 7th AIAA Theoretical Fluid Mechanics Conference, 2014.
[42]L. Salemi, H. Fasel, S. Wernz, and E. Marquart, "Numerical investigation of nonlinear wave packets in a hypersonic high-enthalpy boundary layer on a 5 degree sharp cone," in 45th AIAA Thermophysics Conference, 2015.
[43]L. Salemi and H. Fasel, "Linearized Navier-Stokes simulations of the spatial stability of a hypersonic boundary-layer on a flared cone," in 53rd AIAA Aerospace Sciences Meeting, 2015.
[44]L. Salemi, A. Gross, H. Fasel, S. Wernz, and E. Marquart, "Linearized Navier-Stokes calculations of the spatial stability of a hypersonic boundary layer on a 5° sharp cone with high temperature effects," in 52nd Aerospace Sciences Meeting, 2014.
[45]L. Salemi, "Numerical investigation of hypersonic conical boundary-layer stability including high-enthalpy and three-dimensional effects," Ph.D. thesis, University of Arizona, 2016.
[46]L. Edwards and A. Tumin, "Real gas effects on receptivity to kinetic fluctuations. I. Mean flow effect," AIAA Paper 2017-0070, 2017.
[47]C. Knisely and X. Zhong, "Supersonic modes in hot-wall hypersonic boundary layers with thermochemical nonequilibrium effects," AIAA Paper 2018-2085, 2018.
[48]C. Knisely and X. Zhong, "The supersonic mode and the role of wall temperature in hypersonic boundary layers with thermochemical nonequilibrium effects," AIAA Paper 2018-3218, 2018.
[49]C. H. Mortensen, "Toward an understanding of supersonic modes in boundary-layer transition for hypersonic flow over blunt cones," J. Fluid Mech. **846**, 789–814 (2018).
[50]C. Knisely and X. Zhong, "An investigation of sound radiation by supersonic unstable modes in hypersonic boundary layers," AIAA Paper 2017-4516, 2017.
[51]C. H. Mortensen and X. Zhong, "High-order shock-fitting method for hypersonic flow with graphite ablation and boundary layer stability," AIAA Paper 2012-3150, 2012.
[52]C. H. Mortensen and X. Zhong, "Numerical simulation of graphite ablation induced outgassing effects on hypersonic boundary layer receptivity over a cone frustum," AIAA Paper 2013-0522, 2013.
[53]C. H. Mortensen and X. Zhong, "Real gas and surface ablation effects on hypersonic boundary layer instability over a blunt cone," AIAA Paper 2013-2981, 2013.
[54]C. H. Mortensen and X. Zhong, "Simulation of second-mode instability in a real-gas hypersonic flow with graphite ablation," AIAA J. **52**, 1632–1652 (2014).
[55]C. H. Mortensen and X. Zhong, "Numerical simulation of hypersonic boundary-layer instability in a real gas with two-dimensional surface roughness," AIAA Paper 2015-3077, 2015.
[56]C. Park, *Nonequilibrium Hypersonic Aerothermodynamics* (John Wiley & Sons, Inc., NY, 1990).
[57]J. Lee, "Basic governing equations for the flight regimes of aeroassisted orbital transfer vehicles," in *Thermal Design of Aeroassisted Orbital Transfer Vehicles*, edited by H. F. Nelson (AIAA, 1985), Vol. 96, pp. 3–53.
[58]F. Blottner, M. Johnson, and M. Ellis, "Chemically reacting gas viscous flow program for multi-component gas mixtures," Technical Report No. SC-RR-70-754, Sandia National Laboratories, 1971.
[59]C. Wilke, "A viscosity equation for gas mixtures," J. Chem. Phys. **18**, 517–519 (1950).
[60]X. Zhong, "High-order finite-difference schemes for numerical simulation of hypersonic boundary-layer transition," J. Comput. Phys. **144**, 662–709 (1998).

[61]Y. Liu and M. Vinokur, "Nonequilibrium flow computations. I. An analysis of numerical formulations of conservation laws," J. Comput. Phys. **83**, 373–397 (1989).
[62]J. Williamson, "Low-storage Runge-Kutta schemes," J. Comput. Phys. **35**, 48–56 (1980).
[63]M. Malik and R. Spall, "On the stability of compressible flow past axisymmetric bodies," J. Fluid Mech. **228**, 443–463 (1991).
[64]M. R. Malik, "Numerical methods for hypersonic boundary layer stability," J. Comput. Phys. **86**, 376–413 (1990).
[65]C.-L. Chang, M. Malik, and M. Hussaini, "Effects of shock on the stability of hypersonic boundary layers," in 21st AIAA Plasma Dynamics and Lasers Conference, 1990.
[66]Y. Ma and X. Zhong, "Receptivity of a supersonic boundary layer over a flat plate. II. Receptivity to free-stream sound," J. Fluid Mech. **488**, 79–121 (2003).
[67]Y. Ma and X. Zhong, "Receptivity of a supersonic boundary layer over a flat plate. III. Effects of different types of free-stream disturbances," J. Fluid Mech. **532**, 63–109 (2005).
[68]A. Fedorov and A. Khokhlov, "Excitation of unstable modes in a supersonic boundary layer by acoustic waves," Fluid Dyn. **26**, 531–537 (1991).
[69]A. Fedorov and A. Khokhlov, "Prehistory of instability in a hypersonic boundary layer," Theor. Comput. Fluid Dyn. **14**, 359–375 (2001).
[70]A. Fedorov, "Receptivity of a high-speed boundary layer to acoustic disturbances," J. Fluid Mech. **491**, 101–129 (2003).
[71]V. Gushchin and A. Fedorov, "Excitation and development of unstable disturbances in a supersonic boundary layer," Fluid Dyn. **25**, 344–352 (1990).
[72]C. P. Knisely and X. Zhong, "Sound radiation by supersonic unstable modes in hypersonic blunt cone boundary layers. I. Linear stability theory," Phys. Fluids **31**, 024103 (2019).